The Astrophysical Journal Supplement Series, 284:31 (23pp), 2026 May https://doi.org/10.3847/1538-4365/ae48ec

The First Systematic Survey of Stellar Halos in High-inclination Galaxies Reveals Unusually Quiescent Merger Histories of Nearby Galaxies

Bojun Tao[1,2], Hong-Xin Zhang[1,2,11], Wenting Wang[3,4], Enci Wang[1,2], Guangwen Chen[5,6,7], Huiyuan Wang[1,2], Lijun Chen[1,2], Qian-Hui Chen[8,9], Song Huang[10], Xu Kong[1,2], and Yu Rong[1,2]
[1] Department of Astronomy, University of Science and Technology of China, Hefei, Anhui 230026, People's Republic of China; hzhang18@ustc.edu.cn
[2] School of Astronomy and Space Science, University of Science and Technology of China, Hefei, Anhui 230026, People's Republic of China
[3] Department of Astronomy, Shanghai Jiao Tong University, Shanghai 200240, People's Republic of China
[4] State Key Laboratory of Dark Matter Physics, Key Laboratory for Particle Astrophysics and Cosmology (MOE) and Shanghai Key Laboratory for Particle Physics and Cosmology, Shanghai Jiao Tong University, Shanghai 200240, People's Republic of China
[5] Sub-department of Astrophysics, University of Oxford, Keble Road, Oxford, OX1 3RH, UK
[6] Instituto de Astrofísica de Canarias, calle Vía Láctea s/n, E-38205 La Laguna, Tenerife, Spain
[7] Departamento de Astrofísica, Universidad de La Laguna, Avenida Astrofísico Francisco Sánchez s/n, E-38206 La Laguna, Spain
[8] Research School of Astronomy & Astrophysics, Australian National University, Canberra, 2611, Australia
[9] ARC Centre of Excellence for All Sky Astrophysics in 3 Dimensions (ASTRO 3D), Australia
[10] Department of Astronomy, Tsinghua University, Beijing 100084, People's Republic of China
Received 2025 October 8; revised 2026 February 10; accepted 2026 February 19; published 2026 May 7

Abstract

Stellar halos are the only major stellar component of disk galaxies that lack systematic observational characterization, yet they encode critical information about galaxy merger histories. We present the first systematic census of stellar halos in a large, flux-limited sample of 169 high-inclination central galaxies with stellar masses $7.3 \leqslant \log M_\star/M_\odot \leqslant 11.0$ and redshift $z < 0.1$, using Hyper Suprime-Cam Subaru Strategic Survey Deep optical images. Stellar halos are detected in 93 galaxies, primarily through their low isophotal ellipticities in the outskirts, improving upon conventional methods of stellar halo identification. The halo detection rate reaches ∼50% at $\log M_\star/M_\odot > 9.9$ and $\gtrsim$70% for Milky Way (MW)-mass galaxies. We derive halo surface brightness profiles, colors, and masses, finding that stellar halos generally follow power-law radial profiles. Higher-mass galaxies, on average, exhibit smaller power-law indices and larger halo mass fractions, indicating more extended halos and more active merger histories. A significant stellar halo color–mass correlation, driven mainly by the mass–metallicity relation, suggests dominance by a few massive accretion events. MW-mass galaxies have a median stellar halo fraction of $10\% \pm 5\%$. Among nearby galaxies with halo measurements within 25 Mpc, two-thirds (including the MW) lie below the mean stellar halo fraction–galaxy mass relation. Overall, the nearby galaxies show a median halo deficit of ∼0.3 dex, implying unusually quiescent merger histories. We show that this deficit follows a broader trend in which typical halo fractions increase with heliocentric distance, tracking the gradual rise in matter density toward the cosmic average by $z \lesssim 0.07$.

Unified Astronomy Thesaurus concepts: Galaxy formation (595); Galaxy stellar halos (598); Galaxy structure (622); Stellar populations (1622); Galaxy photometry (611)

Materials only available in the online version of record: machine-readable tables

1. Introduction

According to the standard Lambda cold dark matter cosmological model, galaxies form near the centers of dark matter halos and grow through accretion along the cosmic web and through mergers with other galaxies (S. D. M. White & M. J. Rees 1978; B. Moore et al. 1999). In this hierarchical framework, galaxy interactions and mergers play an important role in driving the evolution of galaxies, especially during the early cosmic epoch. Galaxies that are fully or partially disrupted during mergers contribute to the buildup of stellar halos in the merger remnants (J. S. Bullock & K. V. Johnston 2005; A. P. Cooper et al. 2010).

Cosmological simulations suggest that stellar halos—characterized by relatively long dynamical timescales (J. S. Bullock & K. V. Johnston 2005) and high ex situ stellar fractions (A. S. Font et al. 2011)—act as relics of galaxies' hierarchical assembly histories. State-of-the-art hydrodynamical simulations (A. P. Cooper et al. 2010; L. Oser et al. 2010; J. Wang et al. 2011; C. N. Lackner et al. 2012; A. P. Cooper et al. 2013; A. Pillepich et al. 2014; A. P. Cooper et al. 2015; V. Rodriguez-Gomez et al. 2016; R. D'Souza & E. F. Bell 2018a; G. S. Karademir et al. 2019; B. W. Keller 2022; M. P. Rey & T. K. Starkenburg 2022; R. Shi et al. 2022; A. Genina et al. 2023; E. Angeloudi et al. 2024; S. E. Grimozzi et al. 2024; A. P. Cooper et al. 2025), such as the Illustris (V. Rodriguez-Gomez et al. 2016) and IllustrisTNG (R. Shi et al. 2022; E. Angeloudi et al. 2024) simulations, showed that the fraction of stars formed ex situ (and thus the stellar halo mass fraction) strongly depends on galaxy stellar mass and is generally higher in more-massive and elliptical galaxies. Nevertheless, M. P. Rey & T. K. Starkenburg (2022) demonstrated that there is a wide spread (1.5 dex) in stellar halo mass fractions due to the diversity of merging histories. Due to the steep decline of stellar-to-dark-matter halo mass ratio toward the low-mass end, the stellar halos of massive galaxies

[11] Corresponding author.

are expected to primarily consist of stars stripped from a small number of relatively massive satellites (e.g., A. Genina et al. 2023).

Due to their proximity, the stellar halos of the Milky Way (MW) and M31 have been studied in the greatest detail. By counting individual stars and globular clusters, various halo properties have been revealed (A. Helmi 2008), including the dynamical state and stellar orbits (O. J. Eggen et al. 1962; B. W. Carney & D. W. Latham 1986; M. Chiba & T. C. Beers 2000; B. Yanny et al. 2003; D. Carollo et al. 2010; V. Belokurov et al. 2018), age and metallicity (F. D. A. Hartwick 1976; L. Searle & R. Zinn 1978; W. E. Harris & R. Canterna 1979; A. Helmi et al. 1999; R. Ibata et al. 2001; D. B. Reitzel & P. Guhathakurta 2002; I. U. Roederer 2009; D. An et al. 2013; D. Carollo et al. 2016; E. Fernández-Alvar et al. 2017; K. Youakim et al. 2020; A. Viswanathan et al. 2024), and structural properties (L. Woltjer 1975; W. E. Harris 1976; G. W. Preston et al. 1991; R. Racine 1991; C. J. Wetterer & J. T. McGraw 1996; E. F. Bell et al. 2008; B. Sesar et al. 2011; X.-X. Xue et al. 2015; Y. Xu et al. 2018; A. Chen et al. 2023). The stellar halos of the MW and M31 differ significantly in spatial distribution, chemical abundance, and mass (D. B. Reitzel & P. Guhathakurta 2002; A. J. Deason et al. 2013; B. Harmsen et al. 2017). M31's more-massive halo is thought to have formed through a major merger involving a third galaxy in the Local Group history (F. Hammer et al. 2018). The compact elliptical M32 is likely the remnant bulge of this disrupted galaxy (A. W. McConnachie et al. 2018; R. D'Souza et al. 2018b). The revolutionary discoveries enabled by the Gaia mission revealed that, except for the very central regions, the inner and outer parts of the stellar halos of the MW are each dominantly contributed by a single accreted satellite (e.g., R. P. Naidu et al. 2020), and even the central in situ stellar halos formed by splashed disk population are also intimately linked to past merger events (A. Helmi et al. 1999; E. F. Bell et al. 2008; A. Helmi et al. 2018; J. T. Mackereth et al. 2019; G. C. Myeong et al. 2019; I. Ablimit et al. 2022; M. Xiang & H.-W. Rix 2022; A. J. Deason & V. Belokurov 2024), reinforcing the notion that stellar halos serve as direct tracers of galaxy merger histories.

Stellar halos can be resolved into individual stars only for galaxies within the Local Volume (M. Mouhcine et al. 2005; N. A. Tikhonov & O. A. Galazutdinova 2005; M. Mouhcine et al. 2007; A. Seth et al. 2007; R. Ibata et al. 2009; M. Rejkuba et al. 2009; M. Mouhcine et al. 2010; M. Tanaka et al. 2011; M. B. Peacock et al. 2015; A. Monachesi et al. 2016; E. F. Bell et al. 2017; B. Harmsen et al. 2017; L. Greggio et al. 2018; R. E. Cohen et al. 2020; I. S. Jang et al. 2020; A. Smercina et al. 2020; M. Rejkuba et al. 2022; A. Smercina et al. 2022; K. Gozman et al. 2023; B. Harmsen et al. 2023; A. Smercina et al. 2023). Based on resolved star counts, these studies reveal substantial diversity in stellar halo mass and metallicity, as well as a stellar halo mass–metallicity correlation, among MW-mass galaxies (E. F. Bell et al. 2017; B. Harmsen et al. 2017; A. Smercina et al. 2022). While limited in scope and sample size, the resolved stellar halo studies of these very nearby galaxies provide the gold standard when exploring their unresolved counterparts in more distant galaxies.

Beyond the Local Volume, only the integrated surface brightness distribution of stellar halos can be obtained (P. G. van Dokkum et al. 2014; A. Merritt et al. 2016; I. Trujillo & J. Fliri 2016; C. Gilhuly et al. 2022). These studies found a wide spread in stellar halo fractions for spiral galaxies less massive than the MW, as well as a positive correlation between halo fraction and galaxy stellar mass (A. Merritt et al. 2016; C. Gilhuly et al. 2022). However, these studies are based on incomplete samples within a few tens of Mpc. Furthermore, this very nearby volume appears to have a significantly lower matter density than the cosmic average (R. C. Keenan et al. 2013). Consequently, the stellar halo properties and the galaxy assembly histories they imply may not be representative of the broader local Universe.

Stellar halos typically exhibit surface brightness levels fainter than ∼28–30 mag arcsec^{-2}, necessitating very deep—and thus costly—imaging observations. This imposes severe limitations on sample size and completeness, preventing such studies from yielding statistically meaningful conclusions about stellar halos as an important structural component of galaxies. To circumvent this limitation, stellar halos have also been investigated through image stacking (e.g., S. Zibetti et al. 2004; T. Tal & P. G. van Dokkum 2011; R. D'Souza et al. 2014; W. Wang et al. 2019, 2021a) or surface profile stacking (e.g., D. J. Williams et al. 2024) techniques applied to large samples of galaxies. While stacking enhances the signal-to-noise ratio (S/N) and allows for the measurement of average stellar halo properties out to large galactocentric distances across galaxies of varying masses, it obscures the considerable diversity of stellar halos among individual galaxies, thereby limiting the usability of stellar halos as an indicator of galaxy assembly histories and its connection to other galaxy properties.

Existing deep imaging observations of nearby stellar halos are primarily from two dedicated surveys: Dragonfly Nearby Galaxy Survey with the Dragonfly Telephoto Array (P. G. van Dokkum et al. 2014; A. Merritt et al. 2016) and the LBT Imaging of Galaxy Haloes and Tidal Structures survey (I. Trujillo et al. 2021; D. Zaritsky et al. 2024). The two surveys push the observational boundaries of disk galaxy structures into the stellar halo regime for the first time in a systematic way, using unprecedented deep imaging (30–31 mag arcsec^{-2} in the r or V band) of representative galaxy samples within ∼30 Mpc.

Looking beyond the nearby galaxies, the deep and wide-field coverage of the Hyper Suprime-Cam Subaru Strategic Survey (HSC-SSP; H. Aihara et al. 2018) provides the first opportunity to extend stellar halo studies to a homogeneous and statistically significant sample of galaxies in the broader local Universe, without relying on image stacking. In this work, we utilize the optical images from the HSC-SSP Deep/UltraDeep layers Public Data Release 3 (PDR3; H. Aihara et al. 2022) to characterize the stellar halo properties of individual high-inclination central galaxies in the local Universe ($z < 0.1$).

This paper is organized as follows. Section 2 describes the data and initial sample selection. Section 3.1 details our procedures for removing background/foreground contamination and correcting for point-spread function (PSF) scattering effects. In Section 3.3, we outline the methods used to extract surface brightness profiles along the minor axis, identify stellar halos, and estimate their stellar masses. Our main results are presented in Section 4, and our conclusions are summarized in Section 5.

Throughout this paper, we adopt the first-year Planck cosmology (Planck Collaboration et al. 2014), with a Hubble constant of $H_0 = 67.3\,\mathrm{km\ s^{-1}\ Mpc^{-1}}$, matter density $\Omega_m = 0.315$, and cosmological constant $\Omega_\Lambda = 0.685$.

2. Data and Sample

We begin by selecting a parent spectroscopic sample of central galaxies from the Sloan Digital Sky Survey (SDSS) NYU Value-Added Galaxy Catalog (VAGC; M. R. Blanton et al. 2005) and the Fourth Data Release of the Galaxy And Mass Assembly survey (GAMA DR4; S. P. Driver et al. 2022). The selection is limited to galaxies within the redshift range $0.001 < z < 0.1$ and located within the sky area covered by the HSC-SSP Deep/UltraDeep layers. The upper redshift limit is imposed to mitigate the cosmic dimming effect. We then retrieve and analyze the corresponding PDR3 imaging data. The remainder of this section provides further details on the data sources and sample selection.

2.1. Selection of Isolated Central Galaxies

The parent spectroscopic sample is selected from VAGC and GAMA DR4. For VAGC, we use the postredshift sample all0 as our starting point. The VAGC spans a redshift range from 0.001–0.4 and includes galaxies with r-band apparent magnitude brighter than 17.77 mag. GAMA DR4 covers a broader redshift range and reaches a deeper flux limit of 19.9 mag in the r band. To ensure consistency between the two datasets, we restrict our GAMA sample to galaxies with r-band magnitudes brighter than 17.77 mag. The parent catalogs provide stellar masses of the galaxies, based on spectral energy distribution modeling of multiband photometry, including that from the SDSS images. Recent studies (M. Bernardi et al. 2013; R. D'Souza et al. 2015) demonstrated that the standard SDSS photometry tends to underestimate total galaxy light (and thus stellar mass), missing the outer low-surface brightness regions. Indeed, the SDSS photometry is systematically fainter than our measurements from the HSC-SSP images for galaxies with $\log M_\star/M_\odot < 9$. We therefore derive the stellar masses of these low-mass galaxies using the HSC-SSP r-band luminosity and $g - r$ color, based on the $(g - r)$–mass-to-light ratio (M/L) relation calibrated for local dwarf galaxies by H.-X. Zhang et al. (2017). We verified that adopting different mass estimation methods for low- and high-mass galaxies does not introduce systematic bias by comparing stellar masses derived from both methods for the high-mass subsample.

We select isolated central galaxies from the parent sample by largely following the methodology of W. Wang et al. (2021a). In particular, an isolated central galaxy is (1) the brightest in the r band within $R_{\rm vir}$ and $3 \times V_{\rm vir}$ of itself, and (2) outside of $R_{\rm vir}$ and $3 \times V_{\rm vir}$ of any other more-massive galaxies, and (3) for that from the VAGC sample, without a brighter photometric companion (see below for details), where $R_{\rm vir}$ is the virial radius of host dark matter halos, and $V_{\rm vir}$ is the virial velocity. Both $R_{\rm vir}$ and $V_{\rm vir}$ are derived using the abundance-matching relation from Q. Guo et al. (2010).

The SDSS spectroscopic survey is affected by the "fiber-collision" problem, where two fibers cannot be placed closer than 55″, potentially leading to missed massive companions that lack spectroscopic redshift measurements. To mitigate this potential issue, in addition to the spectroscopic-based selection, we utilize the photometric redshift catalog Photoz2 from SDSS DR7 to exclude galaxies that have a brighter photometric companion whose redshift probability distribution has more than a 10% chance of matching the spectroscopic redshift of the candidate central galaxy in question.

Among the above-selected isolated central galaxies, 978 are located within the HSC-SSP Deep layer footprint. We further exclude 164 galaxies that are either undergoing ongoing tidal interactions (based on visual inspection), fall within the PSF halo of bright stars (defined as regions with g-band $\mu_{\rm star} < 27.5$ mag arcsec^{-2} around the bright star), lie near the boundary of the HSC-SSP Deep layer footprint (see below), or are significantly contaminated by nearby galaxies or artificial ghosts. Furthermore, our focus in this work is on nearly edge-on galaxies, because these galaxies offer ideal viewing angles for probing stellar halos above the disk plane. Therefore, we perform a preliminary visual inspection to exclude 565 (nearly) face-on systems. Applying all of the above selection criteria, we obtain a sample of 249 isolated inclined central galaxies.

2.2. HSC-SSP Deep Survey Images

The HSC-SSP Deep layer covers approximately 27 deg^2 in the optical and near-infrared (NIR) g, r, i, z, and y broadband filters, achieving an r-band imaging depth of ∼27 mag for point sources and a median i-band seeing of 0.″6. The HSC-SSP UltraDeep layer, which spans 3.5 deg^2, is embedded within the deep layer's sky coverage and reaches about 0.6 mag deeper in imaging depth. Our analysis focuses on the g, r, and i bands. The deep layer was designed to overlap with four of the most extensively observed high-Galactic-latitude fields (∼7 deg^2 each): the SXDS+XMM-LSS field, the COSMOS field, the ELAIS-N1 field, and the DEEP2-3 field.

2.3. Excluding Galaxies with Inadequate Surface Brightness Depth

Due to spatial inhomogeneities in instrumental scattering,[12] large-scale flat-fielding uncertainties, and complex light contamination from nearby sources or scattering by cirrus dust in the MW, the local background noise level can vary from galaxy to galaxy. To maintain the quality of our stellar halo analysis, we exclude galaxies with insufficient surface brightness depth, defined as twice the local background rms noise. Below, we describe the procedure used to estimate the local background and its rms noise in the HSC-SSP Deep survey images of each galaxy.

Surface photometry in the low-surface-brightness regime is dominated not by the familiar pixel-to-pixel high-frequency noise (e.g., Poisson noise and pixel-scale flat-field errors), but by large-scale background inhomogeneities (i.e., low-frequency noise). To obtain a robust estimate of the local background and its noise, we follow the methodology of A. Gil de Paz & B. F. Madore (2005). In particular, the low-frequency noise term is quantified by dividing the local background region around each galaxy into tens of approximately equal-area sectors for statistical analysis. Further details are provided in the Appendix. Based on this evaluation, we exclude 24 galaxies with g- and r-band surface brightness limits shallower than 29 mag arcsec^{-2} from subsequent analysis. The retained sample of 225 inclined central galaxies

[12] This effect has been largely corrected in the HSC-SSP data releases since DR2.

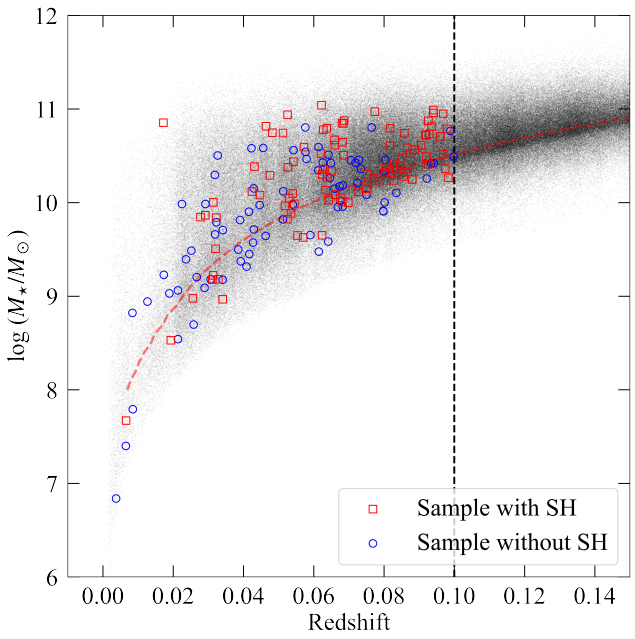

Figure 1. Distribution of our galaxies on the stellar mass–redshift plane. The background gray dots show the parent spectroscopic sample from SDSS DR7 and GAMA DR4, limited to galaxies with $r < 17.77$ mag. Blue open circles represent high-inclination central galaxies without stellar halo detections, while red open squares mark galaxies with stellar halo detections. The vertical dashed line indicates the upper redshift limit applied in our sample selection. The red dashed curve represents the 95% completeness limit of our parent sample of central galaxies. Stellar masses plotted here are all taken from the parent catalogs.

has a median r-band surface brightness limit of $\sim$29.9 mag arcsec^{-2}.

2.4. The Final Sample of High-inclination, Isolated Central Galaxies

Finally, we perform isophotal fitting on galaxy images corrected for PSF-scattered light (Section 3.1.4) to measure the average axial ratio ($q_{\rm disk}$) of isophotes within disk-dominated regions, defined as the radial interval near the minimum of the radial axial-ratio profile. From the 225 galaxies selected above, we then require $q_{\rm disk} < 0.4$, yielding a final sample of 169 high-inclination galaxies for analysis in this work. The high-inclination criterion of $q \lesssim 0.4$ has been adopted in previous studies (e.g., S. J. Kautsch et al. 2006; J. Favaro et al. 2025). We note that our conclusion in this work, such as the halo detection rate, does change if adopting a more restrictive threshold of $q_{\rm disk} < 0.3$.

Figure 1 shows the redshift–stellar mass distribution of our high-inclination galaxy sample. The sample spans the full redshift and stellar mass range of the complete spectroscopic sample from SDSS and GAMA with r-band apparent magnitudes brighter than 17.77 mag. The 95% completeness limit of stellar mass as a function of redshift for the parent spectroscopic sample is also indicated (as red dashed curve) in Figure 1. Figure 2 presents HSC-SSP cutout images of nine representative galaxies from our sample, selected to cover a range of stellar masses and stellar halo fractions. These nine galaxies will be used in the following sections to illustrate the image processing procedures and surface brightness profile extraction applied to the full sample.

3. Methods

In this section, we elaborate on the methods used to process HSC-SSP images and to extract the surface brightness profiles of the stellar halos of our galaxies.

3.1. Image Processing

3.1.1. Wide-PSF Construction and Bright-star Subtraction

As demonstrated in previous studies (R. S. de Jong 2008; T. Tal & P. G. van Dokkum 2011; C. Sandin 2014; I. Trujillo & J. Fliri 2016; W. Wang et al. 2019; C. Gilhuly et al. 2022), the PSF generally has extended wings that scatter light from bright sources (e.g., stars, galaxy bulges) over large angular scales, which can significantly bias surface photometry of extended diffuse structures such as galaxy stellar halos (see Figure 2). To obtain reliable surface brightness profiles in the galaxy outskirts, this scattered light contamination from the PSF wings must be carefully modeled and subtracted. The HSC-SSP survey team provides PSF images across the surveyed field, but these include only the central few arcseconds (see the cyan profile in Figure 3), dominated by atmospheric turbulence, while missing the extended wings of the PSF. Below, we describe our strategy for constructing wide-PSF models that capture the wings for the HSC-SSP Deep layer in the g, r, and i bands.

The PSF images provided by the HSC-SSP team are constructed from unsaturated stars, which do not have sufficient signal-to-noise to reach the extended PSF wings. We construct the wide PSF using a nonparametric method that combines stacked profiles of both unsaturated and centrally saturated bright stars, broadly following the procedure outlined in W. Wang et al. (2019).

We use the Gaia EDR3 catalog (Gaia Collaboration et al. 2016, 2021) to select bright stars for creating wide PSFs within the HSC-SSP Deep layer footprint. For all Gaia sources with $G < 20$ mag, we retrieve coordinates, parallaxes, proper motions, G magnitudes, and BP $-$ RP colors. To exclude potential contamination from compact background galaxies or AGNs, we discard sources with parallax $<$0.1 mas (corresponding to $d > 10$ kpc), thereby constructing a relatively clean star sample for stacking. The selected stars are crossmatched with the HSC-SSP source catalog after correcting their coordinates for proper motion. Because the central pixels of the brightest stars are saturated in HSC images, the integrated fluxes reported by HSC-SSP cannot be used to normalize their images for stacking analysis. To overcome this, we calibrate empirical relations that convert Gaia G magnitude to HSC g-, r-, and i-band PSF magnitude as a function of BP $-$ RP color, using stars with $19 < G < 20$ mag that remain unsaturated in the HSC-SSP images.

We extract HSC-SSP Deep image cutouts centered on the above-selected stars in the magnitude range of $5 < G < 18$ mag. To minimize contamination from background galaxies and other stars, we employ SExtractor to detect and mask the contaminants. We also subtract a sky background separately for each star image.

Brighter stars extend farther into the PSF wings with higher signal-to-noise but may contain more saturated pixels near the center. Following the approach of previous studies (e.g., R. Infante-Sainz et al. 2020), we construct different radial ranges of the wide PSF using stars of different brightness and then combine them into a single wide-PSF image. Specifically,

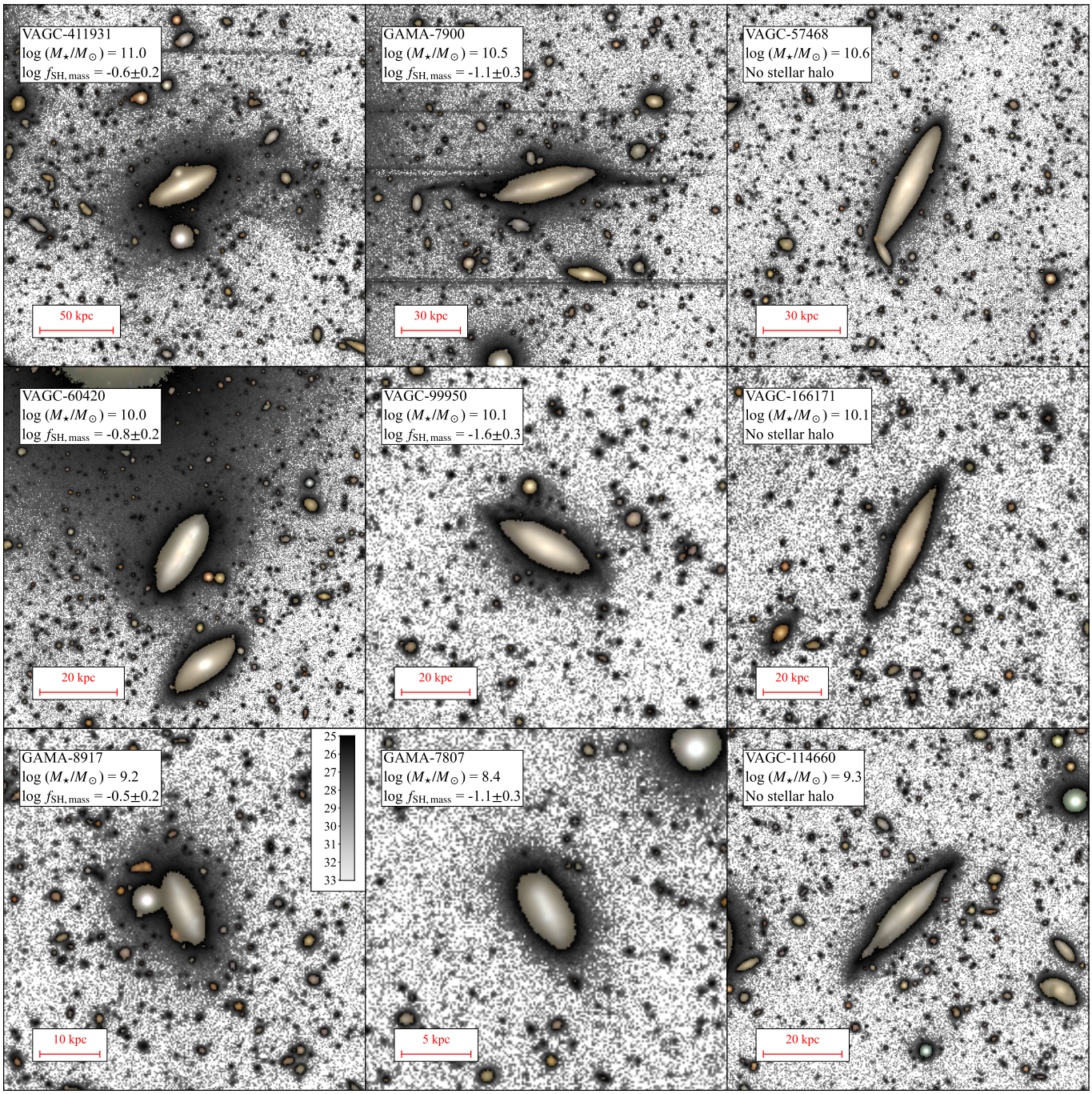

Figure 2. HSC-SSP Deep/UltraDeep images of nine representative galaxies in our final sample of high-inclination central galaxies. For each galaxy, the *g*-, *r*-, and *i*-band tricolor image of the high surface brightness central region is combined with the white-light gray-scale image to reveal the lower surface brightness outskirts. Images are rebinned to enhance visibility of the low-surface-brightness outskirts. The first row shows galaxies with MW-like stellar masses, $\log(M_\star/M_\odot) \sim (10.5,\ 11.0)$. The second row displays galaxies with $\log(M_\star/M_\odot) \sim (10.0,\ 10.5)$. The last row represents galaxies with the lowest stellar masses, $\log(M_\star/M_\odot) < 10.0$. The first column depicts galaxies with high stellar halo fractions, $\log f_{\rm halo} > -1$. The middle column shows galaxies with moderate stellar halo fractions, $\log f_{\rm halo} \sim (-2,\ -1)$. The last column shows galaxies without stellar halo detections. The color bar of the gray-scale image in the lower-left panel is in units of mag arcsec^{-2}.

we divide the sample of bright stars into four magnitude bins ($5 < G < 12$ mag, $12 < G < 14$ mag, $14 < G < 16$ mag, and $16 < G < 18$ mag), and stack normalized, contamination-masked cutouts of stars in each bin separately. Stacking is performed with a 5σ clipped median, and the wing regions are further smoothed with Gaussian kernels to enhance the S/N. Finally, the PSF core provided by the HSC-SSP data team is merged with the four stacked images tracing PSF wings at different radial intervals, yielding the full wide-PSF models in the HSC *g*, *r*, and *i* bands.

The above four stacked PSF wing images generally align with each other at the overlap, nonsaturated part, which makes the combination straightforward. However, we find that the wide-PSF models constructed from stars with $G > 12$ mag differ in their outermost regions from those built with stars with $G < 12$ mag (Figure 3). We therefore designate the

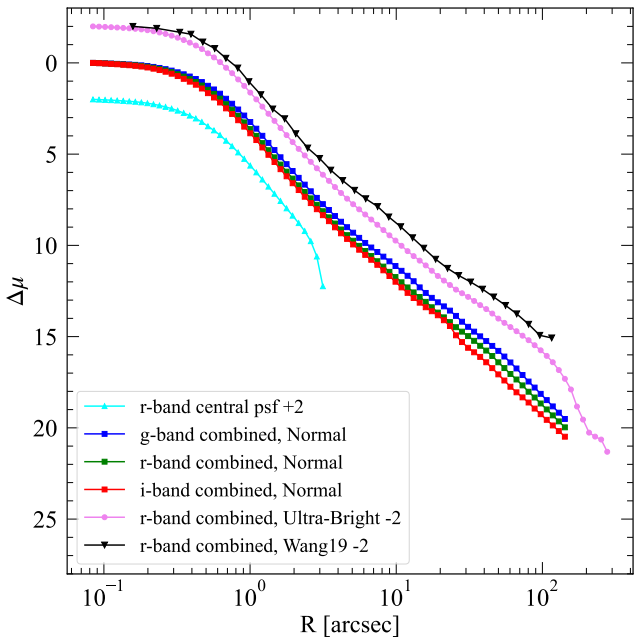

Figure 3. Radial profiles of PSFs constructed for the HSC-SSP Deep/UltraDeep images. Cyan triangles show the *r*-band PSF profile provided by HSC-SSP PDR3, which captures only the PSF core due to atmospheric turbulence but misses the extended PSF wings. The combined "normal" wide-PSF profiles constructed in this work are shown as red squares for the *i* band, green squares for the *r* band, and blue squares for the *g* band. The combined "ultrabright" *r*-band wide-PSF profile is shown as violet circles. For comparison, black triangles represent the *r*-band wide-PSF from W. Wang et al. (2019). See Section 3.1.1 for details.

former as the normal wide-PSF model and the latter as the ultrabright wide-PSF model. The normal wide-PSF model is not sufficiently extended to reach scales beyond $R_{\rm p} \sim 80''$. To address this, we extrapolate the normal model out to $R_{\rm p} \sim 150''$ by fitting a power law, $I_p \propto r^{-n}$, to its surface brightness profile in the range $50 < R_{\rm p} < 80''$ (C. Sandin 2014; Q. Liu et al. 2022). Since all galaxies in our sample are fainter than $G = 12$ mag, we adopt the normal wide-PSF model to correct for PSF scattering from our target galaxies (see below). As shown in Figure 3, the resulting wide-PSF profiles are broadly consistent with those reported by W. Wang et al. (2019) based on the HSC-SSP Wide survey images.

We subtract bright stars contaminating the galaxy images by using the wide-PSF models and Gaia catalog, down to a surface brightness level of $\mu \sim 30$ mag arcsec^{-2}. Specifically, the ultrabright wide-PSF models are applied to stars with $G < 10$ mag, the normal wide-PSF models are applied to stars with $G > 12$ mag, and stars with $10 < G < 12$ mag are modeled using the average of the normal and ultrabright wide-PSF models. Since subtraction residuals often remain in the central regions of bright stars, we mask all areas brighter than $\mu < 27.5$ mag arcsec^{-2} and exclude them from further analysis. Figure 4 shows cutouts of the nine representative galaxies after bright-star subtraction, illustrating the effectiveness of this step in our image processing.

3.1.2. Errors Introduced by Spatial Variations of PSF

While it is necessary to stack a large number of stars to obtain high-quality PSF models, applying a stacked PSF model to the whole field may carry an uncertainty incurred by potential spatial variation of the PSF. For approximately 140 galaxies in our sample, we identified at least five nearby bright stars (with $12 < G < 14$ mag) within a $10'$ radius, enabling the construction of a moderate-quality average PSF model extending to $30''$ for each galaxy. Analysis of these 140 average PSFs reveals that the rms scatter of the normalized profiles increases from 11% at $20''$ to 15% at $30''$.

For a galaxy at a redshift 0.08 (typical for our MW-mass galaxies), a physical scale of 40 kpc (the outermost galactocentric radius adopted for stellar halo measurement; see subsequent sections) corresponds to $\sim 26''$. Within this angular radius, the rms scatter of the PSF is $\leqslant$13%. As demonstrated by W. Wang et al. (2019) using HSC-SSP wide-field images, PSF scattering contributes <50% (10%) of the observed light at a radius of 40 kpc (10 kpc) for galaxies with $\log(M_\star/M_\odot) \geqslant 9.2$. Consequently, subtracting the PSF-scattered light introduces an uncertainty of at most 1% (10% × 13%) and 6.5% (50% × 13%) to the flux measurement at 10 kpc and 40 kpc, respectively. These small uncertainties are negligible compared to other sources of error.

3.1.3. Contaminant Source Masking for Target Galaxies

To accurately extract the light distribution of stellar halos in our target galaxies, it is necessary to first mask foreground and background contaminating objects, in addition to the bright-star subtraction and masking described above. This step is nontrivial because such contaminants span a wide range of angular sizes, morphologies, and separations from the target galaxies. We use SExtractor to detect contaminants in the HSC *g*-, *r*-, and *i*-band cutout images centered on each galaxy, adopting several parameter combinations listed in Table 1. The three key SExtractor parameters are the source detection threshold (`DETECT_THRESH`), the minimum number of contiguous pixels above the threshold (`DETECT_MINAREA`), and the mesh size for background estimation (`BACK_SIZE`). Segmentation maps generated with these settings are then used to mask all objects except the central galaxy itself. Below, we briefly outline the rationale for our mask generation strategy.

In general, a low `DETECT_THRESH` with a large `BACK_SIZE` is required to capture the full extent of an object, but this increases the risk of spurious detections from background noise. To mitigate this, we pair the lowest `DETECT_THRESH` with a relatively large `DETECT_MINAREA` (`segmap_05` in Table 1) and further require that the same objects also be detected with a higher `DETECT_THRESH` and smaller `DETECT_MINAREA` (`segmap_15`). However, this combination does not identify all contaminants, particularly those projected close to the target galaxies. To recover these, we additionally use a series of higher `DETECT_THRESH` values and smaller `BACK_SIZE` (`segmap_20`, `segmap_30`, and `segmap_40`) to detect objects missed in `segmap_05` and `segmap_15`.

The segmentation maps returned by SExtractor cannot capture the full extent of detected objects, even at the lowest detection threshold. To compensate, we expand the segmentation boundaries by 3 and 2 pixels for objects detected in the first two and last three SExtractor runs listed in Table 1, respectively. For larger contaminating companions (HSC $r < 20$ or detected areas comparable to the central galaxy), we further extend the elliptical apertures from `segmap_15` to 2.5 times the R90 (the radius enclosing 90% of the flux). All segmentation maps are then visually inspected and adjusted (if necessary) to ensure that contaminants are fully masked, while

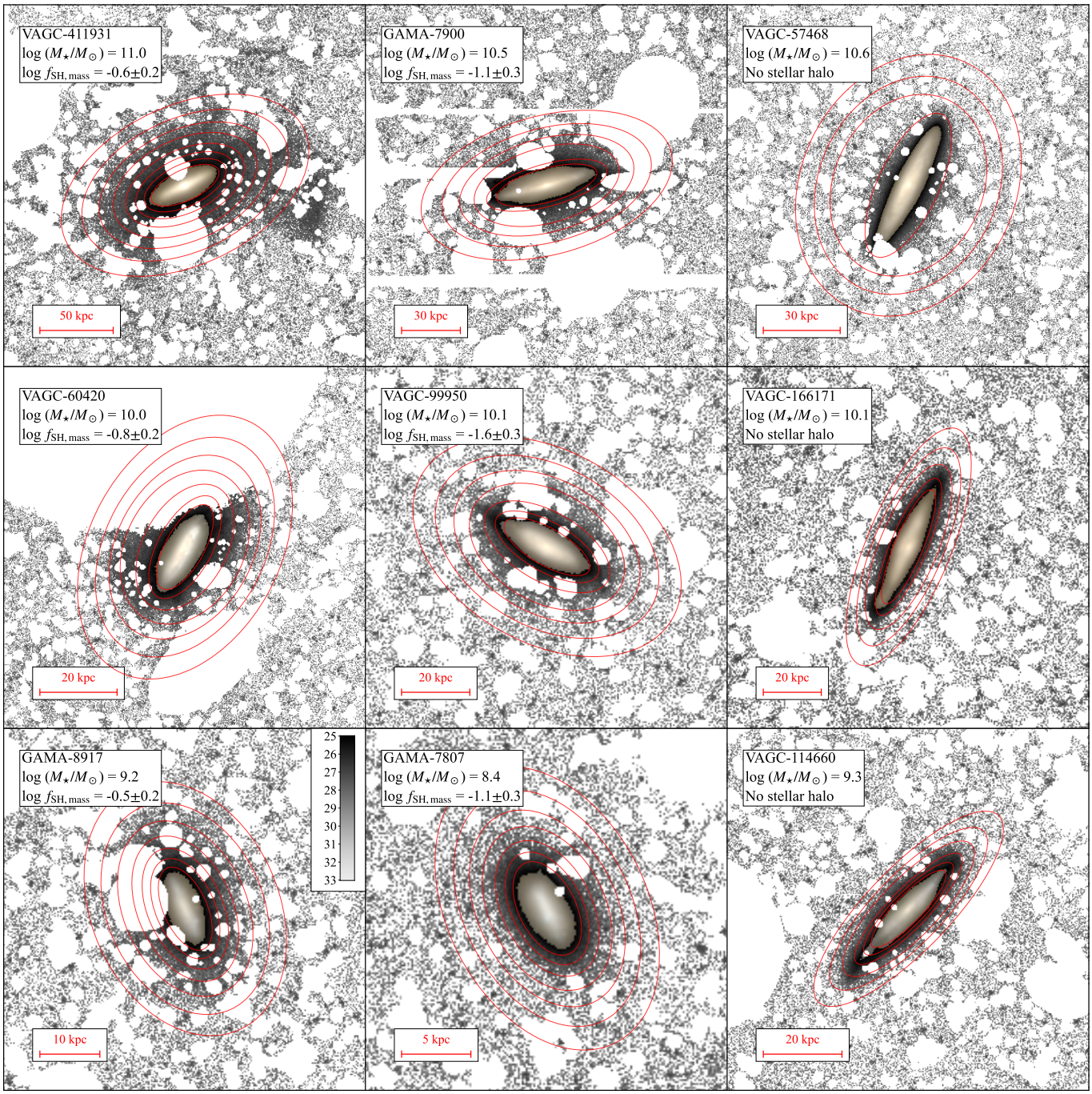

Figure 4. Similar to Figure 2, but after subtracting bright stars and masking contamination sources. Red ellipses show the isophotal contours in the low-surface brightness outskirts. See Sections 3.1.1 and 3.1.3 for details.

spiral arms or other substructures of the target galaxies (if any) are not mistakenly masked, with additional manual masking applied when necessary. The final masks used in our analysis combine these segmentation maps with the bright-star masks described in Section 3.1.1.

3.1.4. Correction of Galaxy Light Profiles for PSF Scattering

The extended wings of the PSF can scatter light from the high-surface-brightness central regions of galaxies into their stellar halos. If uncorrected, this effect can lead to an overestimation of both the stellar halo fraction ($f_{\rm halo}$; W. Wang et al. 2019) and the halo axial ratio (q). To accurately measure the stellar halos of our target galaxies, we adopt a method similar to that of D. Szomoru et al. (2010) and C. Gilhuly et al. (2022) to remove light scattered from the galaxy centers. Specifically, we fit PSF-convolved galaxy models to the observed images with `GALFIT` (C. Y. Peng et al. 2002, 2010), and derive the scattered light as the difference between the best-fit models with and without PSF convolution. The most relevant details of this procedure are described below.

In general, we model galaxy disks using either an exponential profile (a Sérsic model with $n = 1$) or an edge-on disk model. If a prominent bulge is present, an additional

Table 1
SExtractor Parameters for Masking

Name	DETECT_THRESH	DETECT_MINAREA	BACK_SIZE
segmap_05	0.5	25	$2 \times R_{27}$
segmap_15	1.5	4	$2 \times R_{27}$
segmap_20	2.0	4	R_{27}
segmap_30	3.0	4	R_{27}
segmap_40	4.0	4	$0.5 \times R_{27}$

Note. This table lists the most relevant SExtractor parameters used to create contaminant source masks. In the last column, R_{27} denotes the major-axis radius of the isophote with $\mu_r = 27$ mag arcsec^{-2}. See Section 3.1.3 for details.

Sérsic component is included. Because stellar halos contribute only a negligible fraction of the light relative to the disk and bulge in the bright stellar main body, particularly along the major axis, such one- or two-component modeling with GALFIT is not affected by the presence of stellar halos. Upon inspecting the brightness profiles, we find that about 25% of the HSC-SSP Deep *i*-band images of our target galaxies suffer from saturation in their centers, with a few cases also showing saturation in the *r* band. Since the single-exposure time of the Wide survey is much shorter than that of the Deep survey, we use the corresponding Wide survey images for model fitting in these cases. We construct appropriate wide-PSF models applicable to the Wide survey images by retrieving the PSF core images provided by the HSC-SSP Wide survey and combining them with the normal wide-PSF model, joined smoothly at radii of $\sim 1''$–$1.''5$.

GALFIT does not provide a fully holistic framework for structural analysis, and simultaneously fitting multicomponent models can sometimes yield nonphysical solutions, as the model selection is primarily accomplished by minimizing fitting residuals. To obtain reliable disk and bulge models across all bands, we implement a three-step process. In the first step, we mask the potential bulge region and fitted the disk model to the disk region. In the second step, we fix the disk model and used a Sérsic model to fit the bulge. The Sérsic index for the bulge model is set between 2 and 4. Considering that the *i*-band image of HSC-SSP Wide survey has the best seeing quality ($\sim 0.''6$), we use the *i*-band images to determine the morphological parameters of the bulge. In the third step, we fix all of the morphological parameters of the bulge model (center, $R_{e,\mathrm{bulge}}$, n index, q, and PA) and the disk model's center and position angle, leaving other parameters free for fitting the *g*-, *r*-, and *i*-band images, obtaining suitable disk and bulge models. Although accurate measurements of bulge sizes ($R_{e,\mathrm{bulge}}$) are challenging for the most distant galaxies in our sample, the correction for PSF effects remains robust, as demonstrated by D. Szomoru et al. (2010) and D. Szomoru et al. (2012), provided that the residuals do not exhibit systematic biases.

After completing the model fitting, we visually inspect the residuals to identify cases showing systematic deviations from the observation in the central regions. We refine these models by adjusting the three-step procedure mentioned above. For example, in some galaxies with a central deficit instead of excess, the exponential disk fitting caused systematic negative residuals in the central region, so we use a Sérsic model with an index of slightly smaller than 1 to fit the entire galaxy main body. In cases where the bulge occupies a significant fraction of the galaxy, the default bulge mask is insufficient, leading to significant systematic deviations of the model from the observed profile in the center. To improve the fitting to these galaxies, we free both the bulge and disk model parameters in the second step to achieve an optimal fitting result. For few galaxies suffering from central saturation in the HSC-SSP Wide field image in the *i* band, we fit the bulge parameters using the *r*-band image and then used the empirical bulge color of unsaturated galaxies ($r - i \sim 0.41$) to convert the *r*-band bulge model to the *i* band. We mask the saturated central regions of the *i*-band image and fix the bulge component while fitting the disk component.

Using the best-fit two-dimensional galaxy model parameters (disk and bulge components, if present) of our target galaxies, we correct for PSF effects in the Deep field images. With GALFIT, we generate galaxy model images both with and without convolution by the normal wide-PSF model; their difference represents the light scattered by the PSF. Subtracting this difference image from the Deep field data yield the PSF-corrected galaxy images. For galaxies with saturated central regions in the Deep field, the saturated pixels are replaced with the unconvolved galaxy model.

A comparison of the outskirts' ellipticities measured on images with and without subtraction of PSF-induced scattered light is shown in Figure 5, highlighting the importance of correcting for PSF effects when measuring stellar halos. Figure 6 shows processed images of the same nine representative galaxies shown in Figures 2 and 4, after bright-star removal, contaminant masking, and PSF-scattered light subtraction. The change in the light distribution of galaxy outskirts, compared to Figures 2 and 4, is noticeable.

3.2. Extracting Galaxy Surface Brightness Profiles

We use the photutils.isophote.ellipse task to fit elliptical isophotes and extract radial profiles of the azimuthal median surface brightness. The isophotal fitting is performed iteratively. First, we fit elliptical isophotes to white-light images, created as a weighted average of the *g*, *r*, and *i* bands without PSF correction, allowing all geometric parameters to vary with radius. This step determines the average galaxy center based on the best-fit isophotes at intermediate disk radii.

Next, using white-light images produced from PSF-corrected multiband images, we perform ellipse fitting with the center fixed to the value obtained previously, while allowing the axis ratio (q) and position angle (PA) to vary with radius. We ran ellipse with integrmode=median and a fractional step=0.2, and visually inspected the best-fit isophotes to ensure convergence and a smooth radial variation of q and PA. In the third round of ellipse fitting, in addition to fixing the galaxy center, we also fix the PA to the average value measured at the intermediate disk radii where the PA

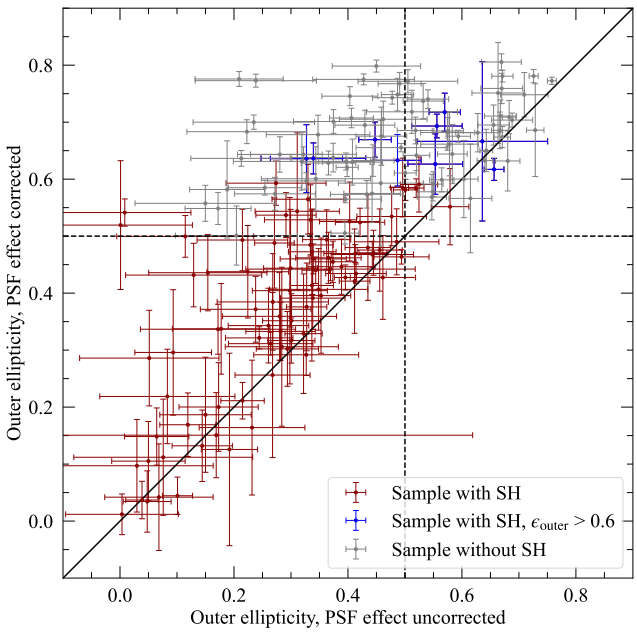

Figure 5. Comparison of the outskirts' ellipticities measured on images with and without subtracting the PSF-induced scattered light. Dark-red circles represent galaxies satisfying the ellipticity threshold (after correcting for the PSF effect) for stellar halo identification, while blue circles represent galaxies with power-law surface brightness profiles in the outskirts but do not satisfy the ellipticity requirement for halo identification (see Section 3.3 for details). Gray circles indicate galaxies without stellar halo detection. This comparison demonstrates the necessity of subtracting PSF-induced scattered light for reliable ellipticity measurements and stellar halo selection.

remains nearly constant. Occasional abrupt jumps in q are manually corrected by replacing them with linearly interpolated values from adjacent isophotes. The convergence threshold and maximum gradient error parameters in `ellipse` are kept at their default settings. We obtain high-quality isophotal fits for the relatively bright disk region in the third `ellipse` run. In the fourth `ellipse` run, we increase the fractional `step` parameter to 0.3 in order to derive reliable ellipticities for the extended and faint outskirts, where the third run fails to converge. The isophotal fits for these faint outer regions are then merged with the converged fits for the bright disk region obtained from the third run. In the outermost regions, where the S/N is insufficient for convergence, the geometric parameters are fixed to those of the nearest converged isophotes. Lastly, to achieve finer radial sampling of the surface brightness profiles than that used for constraining the isophotal geometric parameters, we reduce the fractional step size by a factor of 2, linearly interpolating the best-fit radial variation of the ellipse parameters obtained from the previous fitting.

Finally, we measure the isophotal radial brightness profiles from the PSF-corrected *g*-, *r*-, and *i*-band images separately, fixing all geometric parameters to the previously determined values. Using the `build_ellipse_model` task, these radial profiles are converted into two-dimensional galaxy models. Masked pixels in the galaxy images are replaced with the model values to create "clean" images. These clean images are then used to measure the accumulated flux within elliptical apertures along the semimajor axis, enabling the construction of the curve of growth and the derivation of quantities such as total flux, $R_{\rm e,maj}$, and concentration parameters in each band.

3.3. Stellar Halo Identification and Measurement

Stellar halos are distinguished from the rotation-dominated, flattened galaxy disks by their dispersion-dominated and nearly spheroidal morphology. In high-inclination galaxies, stellar halos can be straightforwardly identified in galaxy images through their large minor-to-major axis ratios, $q_{\rm intr}$ (or equivalently, small ellipticity $\epsilon_{\rm intr} = 1 - q_{\rm intr}$). The isophotal fitting of galaxy images (Section 3.2) provides the radial variation of $q_{\rm intr}$, enabling the identification of radial ranges dominated by the stellar halo.

Previous studies of several Local Volume galaxies based on star counts found that nearly all stellar halos exhibit axis ratios q in the range of ∼0.5–0.8 (see references in the introduction), and q generally increases with galactocentric radius. Using Illustris simulations, L. M. Elias et al. (2018) demonstrated that over 95% of MW-mass galaxies have stellar halos with an intrinsic minor-to-major axis ratio >0.5. This fraction would be even higher when accounting for projection effects. The typical axis ratios of stellar halos have little overlap with those of thick disks in spiral and S0 galaxies ($q \lesssim 0.4$; e.g., J. Favaro et al. 2025), thereby permitting a clear geometric separation.

3.3.1. The Most Prominent Stellar Halos in the Sample

Given the distinct morphologies of stellar halos compared to galaxy disks, we begin our halo identification by focusing on the most prominent stellar halos in the sample. These serve as a guide for developing a more complete identification of halos in our sample. To select the most prominent halos, we impose two criteria: (1) the halo-dominated radial range satisfies $q > 0.5$ (or equivalently, $\epsilon < 0.5$), and (2) the outermost boundary either extends to more than twice the inner boundary or includes no less than seven data points with S/N > 2. The latter criterion ensures a robust discrimination of functional forms of the surface brightness profiles. Together, these two criteria yield a sample of 49 galaxies.

An example illustrating the differentiation of the stellar halo from other galaxy components is shown in Figure 7. In addition to the azimuthally median surface brightness profiles, the figure also shows median profiles measured within 60° wedges centered on the minor axis above and below the disk plane. The wedge profiles provide a cleaner view of the halo, as they are less affected by potential disk contamination near the major axis, albeit at the cost of lower S/N. Since we do not find significant differences between the surface brightness profiles from the two methods, especially in disk or stellar halo dominant regions, we adopt the azimuthally median profiles for the following analysis.

As exemplified in Figure 7, the galaxy is divided into radial ranges dominated by different structural components. The innermost division line (or ellipse) corresponds to the radius of maximum ellipticity, marking the maximum relative contribution of the thin disk. Inside this radius, the bulge component (if present) gradually changes the isophotal ellipticity toward smaller radii, while beyond it, the contribution from the thick disk progressively increases. The outermost division line (or ellipse) is set at $\epsilon = 0.5$, corresponding to the conservative inner boundary of stellar halo-dominated regime. The intermediate division line (or ellipse) marks the radius where the surface brightness profile begins to deviate from the exponential fit at smaller radii, signifying the regime where the stellar halo starts to make a noticeable contribution.

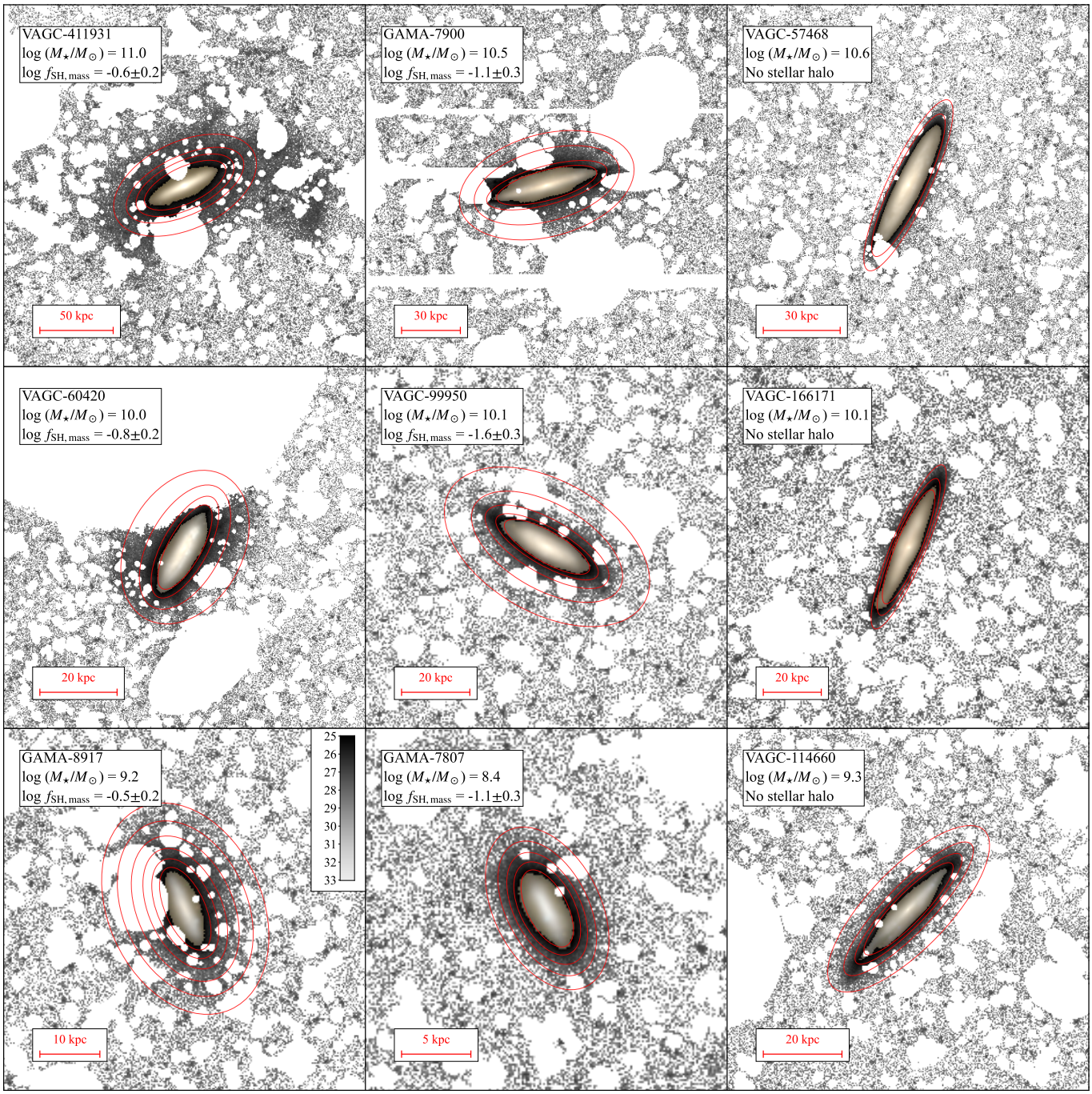

Figure 6. Similar to Figure 2, but after subtracting bright stars, masking out contaminating sources and subtracting PSF-induced scattered light. Red ellipses depict the isophotal contours in lower surface brightness outskirts.

We model the surface brightness profiles of stellar-halo-dominated regions as a function of minor-axis radius using three functional forms: a single power law (SPL), a broken power law (BPL), and an exponential profile. To avoid the profile fitting being dominated by the densely sampled inner regions, we rescale the measurement variances of surface brightness at each radius by the reciprocal of the number of valid pixels in the corresponding elliptical ring. The uncertainties of the model parameters are then estimated with the Markov Chain Monte Carlo method, implemented via the `emcee` sampler. Model selection is performed using the Bayesian information criterion, which balances goodness of fit against model complexity by penalizing the number of parameters. Out of the 49 galaxies in our sample, 38 are best described by the SPL model, six by the BPL model, and only five by the exponential model. The prevalence of power-law profiles is consistent with previous findings for the MW and other nearby galaxies, where more sophisticated halo-star selection techniques have been applied. This agreement not only validates the minor-to-major axis ratio as a robust parameter for identifying stellar-halo-dominated regions, but also confirms that stellar halos generally follow power-law radial profiles.

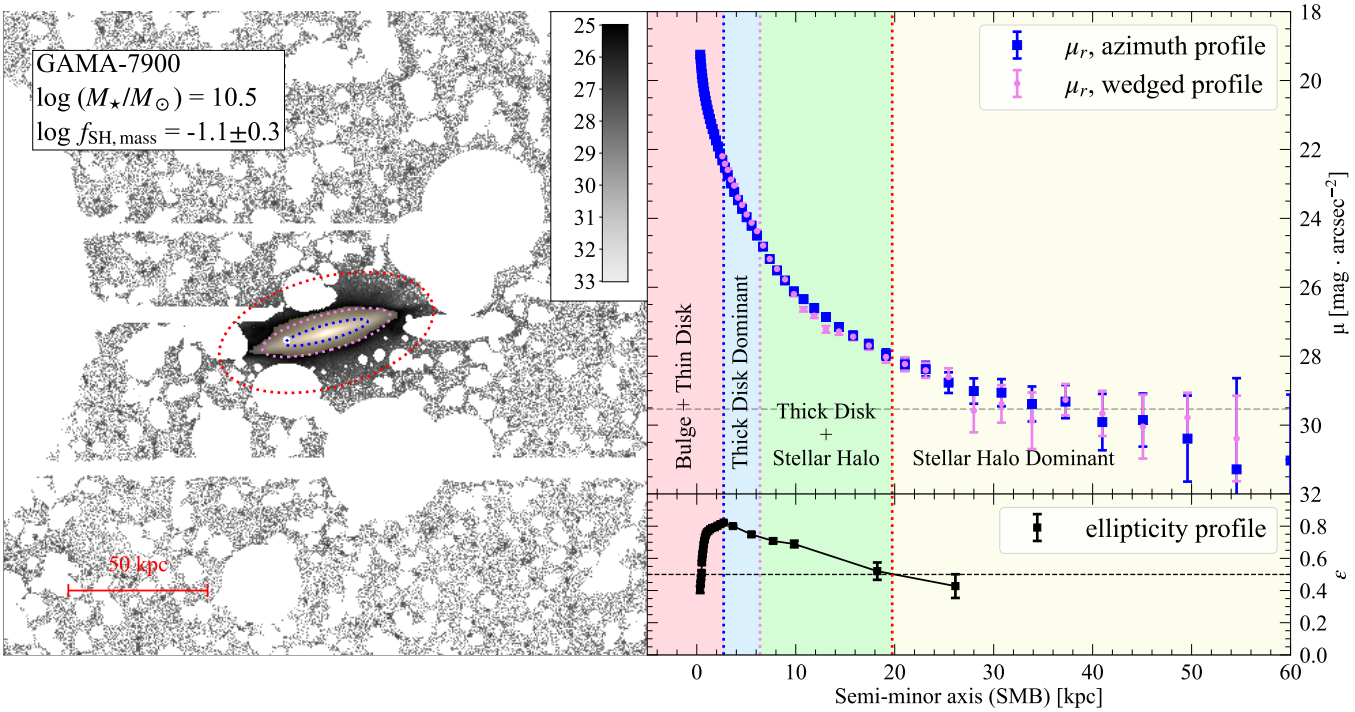

Figure 7. An example of identifying the stellar halo-dominated regions. Left panel: a composite image of a galaxy, produced in a similar way to that shown in Figure 6. Colored dotted ellipses mark the division of the radial ranges dominated by different galaxy components (i.e., bulge, thin disk, thick disk, and stellar halo). Upper-right panel: radial surface brightness profiles along the minor axis. Blue squares with error bars show the azimuthally median profiles, while violet circles represent the median profiles measured within 60° wedges around the minor axis above and below the disk plane. The horizontal dashed line indicates the 2σ surface brightness limit. Vertical dotted lines mark the same division radii as represented by the ellipses in the left panel, using the same color scheme as the ellipses. Lower-right panel: isophotal ellipticity profile. All radial profiles are plotted as a function of galactocentric distance along the semiminor axis (SMB) in kiloparsecs. See Section 3.3.1 for details.

To obtain more precise measurements of stellar halos, we model the surface brightness in the thick-disk-dominated radial ranges with an exponential profile as a function of minor-axis distance, and subtract the best-fit exponential from the observed profile. The thick-disk-dominated region is identified as the radial range exhibiting exponential behavior beyond the peak of the ellipticity radial profile. In cases where no clear exponential radial segment is found beyond the peak, the fitting is performed using data near the peak. The r-band surface brightness profiles for the nine representative galaxies introduced before, along with the corresponding disk-subtracted profiles, are shown in Figure 8. We find that the surface brightness profiles of the 49 most prominent stellar halos remain largely unaffected by the disk component at radial ranges with $q \geqslant 0.4$ (or $\epsilon \leqslant 0.6$), retaining their power-law form.

3.3.2. The Full Sample of Stellar Halos

Based on the lessons learned from the most prominent halos, we establish three joint detection criteria to identify stellar halos in the full sample: (1) the outer radial range satisfies $q > 0.5$ (or $\epsilon < 0.5$); or (2) the outer radial range satisfies $q > 0.4$ (or $\epsilon < 0.6$), and follows a power-law radial decline along the minor axis; or (3) the outskirts remain at $q < 0.4$, but exhibit a power-law radial decline along the minor axis. Applying these criteria, we identify stellar halos in a total of 93 galaxies. Among these, 69 galaxies meet the first criterion, 15 galaxies satisfy the second, and nine galaxies fulfill the third. We note that all stellar halos identified using the first criterion can be well described by a power-law radial profile.

To consistently define an inner boundary of the halo-dominated region in the galaxies identified above, we adopt the minor-axis radius where the halo contribution starts exceeding more than half of the observed light, or equivalently where the surface brightness decreases by less than 0.75 mag arcsec^{-2} after disk subtraction. In practice, we impose a stricter criterion that the surface brightness decrease be less than 0.5 mag arcsec^{-2}, allowing for a 2σ margin, where σ corresponds to the typical measurement uncertainty of 0.12 mag arcsec^{-2} near the halo boundaries of our galaxies. This definition of inner boundaries of stellar-halo-dominated regime is adopted to estimate stellar halo properties in following sections. In Figure 8, the inner boundaries of the nine representative galaxies are each marked by a red vertical dashed line.

Given the overwhelming dominance of single power-law profiles among the 49 most prominent halos, and the limited surface brightness dynamical range in the remaining galaxies of the full sample, we adopt a single power-law model to fit the disk-subtracted stellar halo profiles of all 93 galaxies for consistency, using the same method described in Section 3.3.1. The single power-law model is given by

$$I = I_0 \times \left(\frac{\mathrm{SMB/kpc}}{10\ \mathrm{kpc}}\right)^{-n}, \quad (1)$$

where n is the power-law index, "SMB/kpc" is the semimino r-axis radius in kiloparsecs, and I_0 is the flux at the arbitrarily chosen characteristic radius 10 kpc. Among the 93 galaxies with stellar halo detection, 78 have at least five data points in the stellar halo region in the r band, allowing for a robust single power-law fit. The remaining 15 galaxies have too few

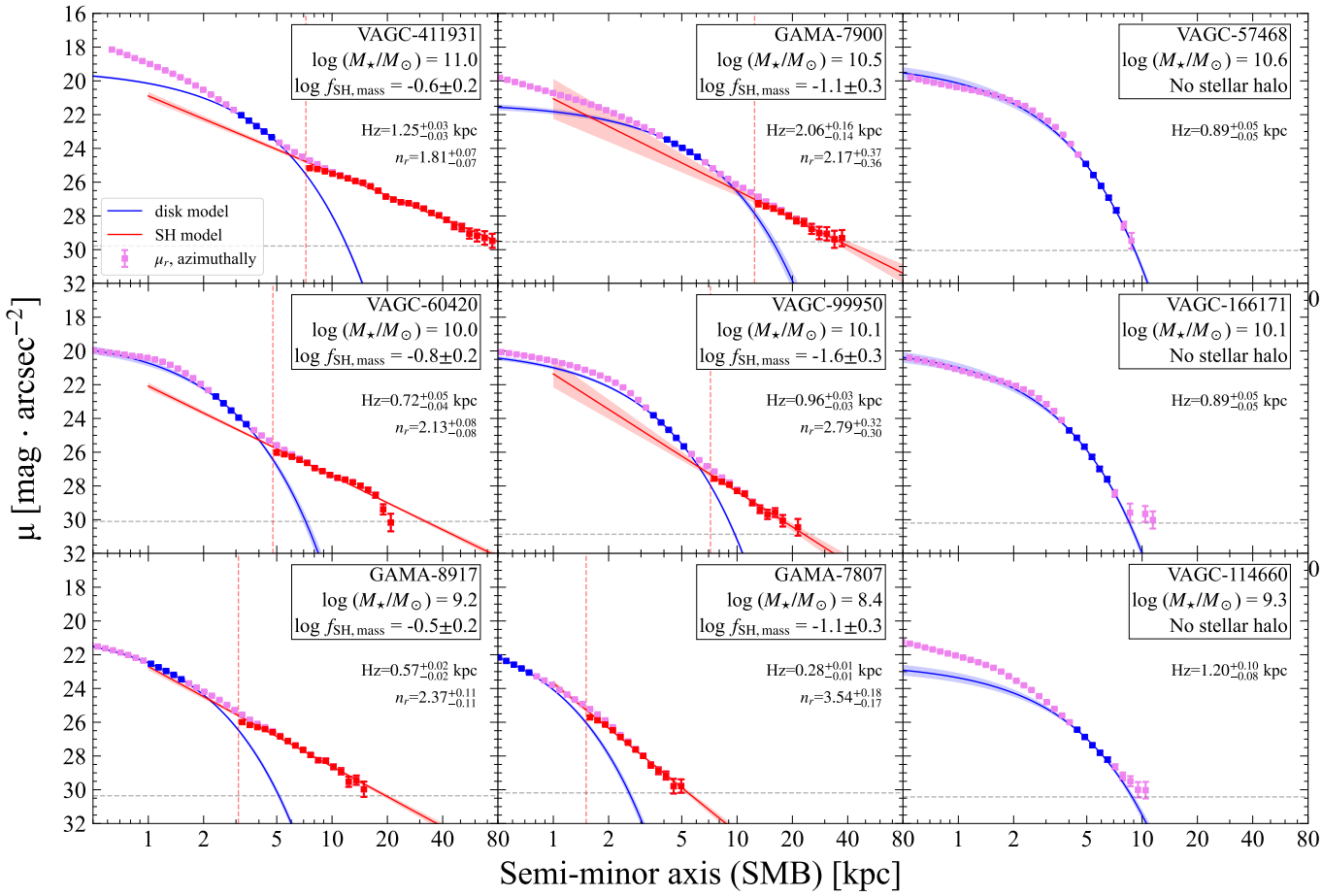

Figure 8. Examples of stellar halo measurements from surface brightness profiles. Each panel shows one of the same galaxies presented in Figure 6. Violet squares with error bars represent the *r*-band azimuthally median surface brightness profiles along the minor axis. Blue squares indicate the outer disk (thick-disk)-dominated region used for fitting an exponential model, with the best-fit exponential overplotted as blue curves. Red squares show the disk-subtracted surface brightness profiles used for power-law fitting (red curves) of the halo-dominated region. The red vertical dashed line marks the inner boundary of the stellar-halo-dominated region adopted for halo profile fitting, and the gray horizontal dashed line indicates the 2σ surface brightness limit. The best-fit thick disk exponential scale height and the stellar halo power-law index are also indicated in each panel. See Section 3.3.2 for details.

data points to constrain both I_0 and n. For the 78 well-sampled halos, we therefore fit both I_0 and n, while for the 15 sparsely sampled cases, we adopt the posterior distribution of n derived from the well-sampled halos as a prior during the fitting.

3.3.3. Estimation of Total Stellar Halo Mass

Stellar halos are expected to extend continuously into the central regions of galaxies, but their profiles can only be reliably constrained in the outskirts where the halo component dominates. Previous studies commonly applied an "aperture correction" factor to scale the observed halo mass to the expected total. By analyzing several different cosmological hydrodynamical simulations (J. S. Bullock & K. V. Johnston 2005; V. Rodriguez-Gomez et al. 2016; A. Monachesi et al. 2019), E. F. Bell et al. (2017) derived a consistent average multiplicative correction factor of 3, scaling the halo mass measured within the minor-axis distance range of 10–40 kpc to the total halo mass for galaxies with stellar masses in the range of 3–10 $\times$ $10^{10}M_\odot$. This factor carries a random scatter of about 40% and a systematic uncertainty below 15%.

To apply this scaling factor to our sample, we first examine how best to normalize the minor-axis profiles of galaxies spanning a wide range of stellar masses and sizes. In Figure 9, we show the minor-axis surface brightness profiles of our galaxies and compare two normalization schemes. In the first, the minor-axis radius of each profile is normalized by its own major-axis half-light radius, $R_{\rm e,maj}$ (upper panels). In the second, the radius is normalized by the average $R_{\rm e,maj}$, denoted $\langle R_{\rm e,maj}\rangle$, of galaxies of similar stellar mass (lower panels). $\langle R_{\rm e,maj}\rangle$ is derived based on a broken log–log linear fit to the LOWESS-smoothed stellar mass–$R_{\rm e,maj}$ relation of our sample, parameterized as

$$\log\langle R_{\rm e,maj}\rangle = k\cdot(\log M_\star/M_\odot - 9.5) + 0.66, \qquad (2)$$

where k is 0.26 for $\log M_\star/M_\odot < 9.5$ and 0.10 for $\log M_\star/M_\odot \geqslant 9.5$. As shown in Figure 9, $\langle R_{\rm e,ma}\rangle$-normalized minor-axis profiles exhibit significantly smaller scatter across the full sample compared to those normalized by each galaxy's own $R_{\rm e,maj}$. The $\langle R_{\rm e,maj}\rangle$-normalized minor-axis profiles of our galaxies display about self-similar shapes.

For the stellar mass range analyzed by E. F. Bell et al. (2017), the minor-axis distance range of 10–40 kpc corresponds to ~2–8 $\times$ $\langle R_{\rm e,maj}\rangle$. We therefore estimate the total stellar halo mass in our galaxies by multiplying "aperture mass" measured within 2–8 $\times$ $\langle R_{\rm e,maj}\rangle$ by a factor of 3.

The stellar halo mass is derived from the *r*-band luminosity and its M/L, obtained using the M/L–($g-r$) relation from H.-X. Zhang et al. (2017). As shown by H.-X. Zhang et al.

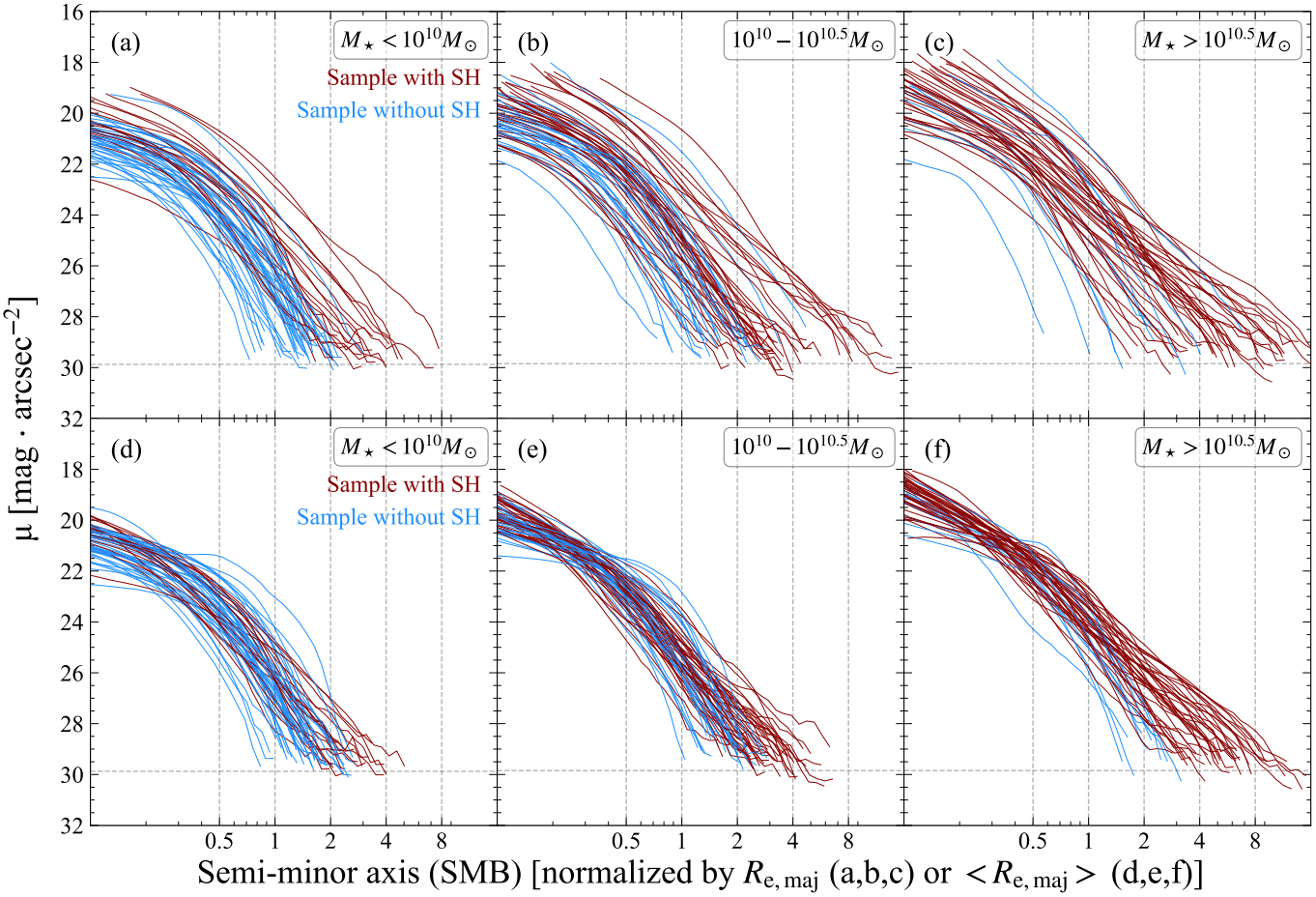

Figure 9. The *r*-band azimuthally median surface brightness profiles along the minor axis of all sample galaxies, shown in units of $R_{\rm e,maj}$ (upper panels) or $\langle R_{\rm e,maj} \rangle$ (lower panels). Galaxies are grouped by stellar mass range in different columns, as indicated in each panel. Here, $R_{\rm e,maj}$ denotes the half-light radius along the major axis, and $\langle R_{\rm e,maj} \rangle$ represents the mass-dependent average $R_{\rm e,maj}$ predicted by a piecewise log–log linear fit to the $R_{\rm e,maj}$–stellar mass relation of our galaxies. Dark-red profiles indicate galaxies with stellar halo detections, while blue profiles indicate galaxies without stellar halo detections. This figure demonstrates that surface brightness profiles normalized by the average major-axis half-light radius exhibit substantially smaller scatter than those normalized by each galaxy's own half-light radius. See Section 3.3.3 for details.

(2017), the M/L–($g - r$) relation is among those with the weakest dependence on star formation history (second only to $B - V$), and is therefore the optimal choice for estimating M/L of our stellar halos. This relation carries a random uncertainty of ∼0.2 dex under conditions of low dust extinction. The $(g - r)_{\rm outer}$ color used for M/L estimation is measured across stellar halo-dominated region of each galaxy. For a few galaxies with very low-S/N measurement of colors, we use the M/L predicted by the best-fit log–log linear relation between M/L and the stellar halo mass of the other galaxies.

4. Results

All basic galaxy properties and derived stellar halo measurements are provided in Tables 2 and 3. Where applicable, reported fluxes and colors have been *K*-corrected to redshift $z = 0$ following I. V. Chilingarian et al. (2010), which presents analytic formulae based on observed colors and redshift.

4.1. Stellar Halo Detection Rate

It goes without saying that the ability to detect stellar halos is limited by the surface brightness depth of the imaging survey. As a result, halo detections are biased toward galaxies with relatively high halo fractions, with this bias becoming more pronounced at lower stellar masses. We quantify the halo detection rate as a function of galaxy stellar mass by adopting a 0.5 dex mass bin width and a 0.1 dex running step for the bin centers, evaluated from the high-mass end to the low-mass end of the sample. The resulting halo detection rate curve is shown in Figure 10. The stellar halo detection rate decreases from ∼90% at the high-mass end to ∼50% at stellar masses $\log(M_\star/M_\odot) \sim 9.9$, below which it declines rapidly and reaches a plateau of ∼30% (with significant fluctuation) at $\log(M_\star/M_\odot) < 9.7$. A detection rate below 50% makes it challenging to recover typical properties of the underlying population. We therefore restrict our subsequent statistical analyses to galaxies with $\log(M_\star/M_\odot) > 9.9$.

4.2. Power-law Indices of Stellar Halo Profiles

Figure 11 presents the power-law indices *n* fitted to the mino r-axis stellar halo profiles in the *g*, *r*, and *i* bands as a function of the stellar mass for galaxies with well-sampled halo profiles (78 in the *r* band). While our sample includes galaxies with $\log(M_\star/M_\odot)$ down to ≃7.0, we focus on galaxies with $\log(M_\star/M_\odot) > 9.9$.

Table 2
Basic Properties of High-inclination Central Galaxies

Name	R.A. (J2000) (deg)	Decl. (J2000) (deg)	Redshift	$\log(M_*)$ ($M_\odot$)	m_r	R_e (kpc)	C_{28}	f_{bulge}	ϵ_{outer}
(1)	(2)	(3)	(4)	(5)	(6)	(7)	(8)	(9)	(10)
Galaxies with stellar halo detection									
VAGC-13467	151.05717	+0.81246	6.2e-02	11.04	14.95	8.15	4.44	−0.80	0.15 ± 0.05
VAGC-411931	352.78012	−1.21441	9.4e-02	10.99	15.90	7.05	5.43	−0.66	0.43 ± 0.02
GAMA-18375	36.66859	−4.38636	7.7e-02	10.97	15.52	12.74	3.18	−1.26	0.64 ± 0.03
…	…	…	…	…	…	…	…	…	…
GAMA-628	34.25908	−5.06413	2.6e-02	8.95	16.90	1.78	3.53	−1.07	0.17 ± 0.06
GAMA-7807	35.85556	−5.64420	1.9e-02	8.43	17.67	1.43	2.29	…	0.39 ± 0.05
VAGC-96050	150.24617	+3.46430	6.6e-03	8.34	15.95	2.85	2.79	…	0.44 ± 0.02
Galaxies without stellar halo detection									
VAGC-411901	350.41335	−1.15126	7.6e-02	10.80	15.87	23.21	2.11	−2.06	0.80 ± 0.01
VAGC-527160	353.51266	+0.36529	5.8e-02	10.80	15.35	4.01	4.95	−0.39	0.69 ± 0.03
VAGC-57421	148.66273	+1.80068	9.9e-02	10.77	16.74	5.56	5.04	−0.79	0.68 ± 0.05
…	…	…	…	…	…	…	…	…	…
VAGC-166177	352.75864	−0.13193	8.5e-03	8.02	16.88	1.51	2.33	…	0.71 ± 0.03
VAGC-57424	148.68743	+1.60949	6.5e-03	7.78	16.92	1.13	2.61	…	0.60 ± 0.02
VAGC-60459	151.10460	+2.55873	3.8e-03	7.33	16.89	0.78	3.11	…	0.63 ± 0.02

Note. This table summarizes the basic properties of our high-inclination central galaxies, grouped according to whether a stellar halo is detected and sorted by galaxy stellar mass. Columns: (1) galaxy name; (2) R.A. (J2000); (3) decl. (J2000); (4) redshift; (5) galaxy stellar mass; (6) r-band magnitude; (7) half-light radius along major axis; (8) concentration; (9) bulge fraction; (10) outer ellipticity. All properties are measured in imaging data corrected for PSF-induced scatter light. All colors and mass are K-corrected and Galactic-extinction-corrected. The uncertainties represent the 1σ confidence level.

(This table is available in its entirety in machine-readable form in the online article.)

The median and central 68% scatter of the n-distributions for each band are reported in the upper-right corner of each panel. A weak but systematic dependence of the median n on wavelength is observed, such that the median n is larger in redder filters. This slight wavelength dependence indicates that stellar halo profiles are steeper at longer wavelengths, implying negative median color gradients in the stellar halos.

We perform a Spearman rank correlation test of the galaxy mass dependence of n, and find a weak ($-0.2 \leqslant \rho \leqslant -0.1$) negative correlation. We perform a linear fit to the relations. The best-fit slopes and intercepts are reported in each panel. The negative galaxy mass dependence of n suggests that the stellar halos of more-massive galaxies tend to have a more extended spatial distribution.

To place our findings in context, we compare the stellar halo profiles of our sample with those of the MW and other nearby galaxies. To make the comparison, we first convert the three-dimensional power-law indices reported in previous studies to projected values by subtracting 1. The projected power-law index of the MW reported in the literature spans a range of 1.5–2.5 (E. F. Bell et al. 2008; M. Jurić et al. 2008; L. L. Watkins et al. 2009; A. J. Deason et al. 2011; B. Sesar et al. 2011; B. Pila-Díez et al. 2015; X.-X. Xue et al. 2015; P. Das et al. 2016; I. Ablimit & G. Zhao 2018; G. Iorio et al. 2018; C. Yang et al. 2022; A. Chen et al. 2023; G. E. Medina et al. 2024), which overlaps with the typical values of our sample. For M31, the power-law index is ∼2.6–2.7 (R. A. Ibata et al. 2014; B. F. Williams et al. 2015), in good agreement with the median of our sample. B. Harmsen et al. (2017) reported power-law indices ranging from 2.0–3.7 for six nearby MW-mass galaxies from the GHOSTS survey, while C. Gilhuly et al. (2022) found n values between 1.7 and 3.3 for 11 out of 12 nearby edge-on disk galaxies. Overall, these literature measurements fall within the range spanned by our sample.

4.3. Colors of Stellar Halos

Figure 12 presents the integrated colors, $(g-r)_{halo}$, $(g-i)_{halo}$, and $(r-i)_{halo}$ of the stellar halos as a function of the galaxy stellar mass. Nine galaxies with color S/N < 3 were not plotted.

The median and central 68% scatter of the three colors are reported in the upper-right corner of each panel. The colors of $(g-r)_{halo}$ and $(g-i)_{halo}$ have a moderate ($\rho \sim 0.25$) and significant (p-values $\leqslant 0.05$) correlation with galaxy stellar mass, suggesting redder median colors of more-massive galaxies. Linear least-squares fitting was performed for the color–mass distribution, and the best-fit slopes and intercepts are reported in the figure.

A. Merritt et al. (2016) reported $g-r$ colors ranging from 0.40–0.75 within 10–20 kpc along the major axis of six nearby galaxies from the Dragonfly Nearby Galaxies Survey. W. Wang et al. (2019) reported $g-r$ colors between 0.3 and 0.8 and $g-i$ colors between 0.6 and 1.2 within 10–20 kpc by stacking isolated central galaxies with total stellar masses of $10^{9.2}$–$10^{11.1}\,M_\odot$ at redshift 0.05–0.1. They also found a clear positive stellar mass dependence of the colors. C. Gilhuly et al. (2022) measured average outskirts' $g-r$ colors of 0.40–0.75 for 12 nearby edge-on disk galaxies with stellar masses in the range $10^{9.68}$–$10^{10.88}\,M_\odot$. All of these previous color measurements occupy a color range similar to that found in our work. The redder typical colors of stellar halos in more-massive galaxies reflect either older stellar ages or, more importantly, higher metallicities (see also Section 4.5).

Table 3
Stellar Halo Properties of High-inclination Central Galaxies

Name	$(g-r)_{\rm halo}$	$(g-i)_{\rm halo}$	$(r-i)_{\rm halo}$	$\log {\rm M/L}_{\rm outer}$ $(M_\odot/L_\odot)$	$n_{\rm g}$	$n_{\rm r}$	$n_{\rm i}$	$\log(f_{\rm SH,mass})$	$\log(f_{\rm SH,flux})$
(1)	(2)	(3)	(4)	(5)	(6)	(7)	(8)	(9)	(10)
Galaxies with stellar halo detection									
VAGC-13467	0.55 ± 0.05	0.92 ± 0.03	0.37 ± 0.04	0.12 ± 0.16	2.56 ± 0.09	2.81 ± 0.09	2.65 ± 0.07	−0.88 ± 0.23	−0.71 ± 0.02
VAGC-411931	0.69 ± 0.04	0.98 ± 0.04	0.29 ± 0.03	0.28 ± 0.16	1.74 ± 0.09	1.81 ± 0.07	1.76 ± 0.06	−0.58 ± 0.23	−0.59 ± 0.02
GAMA-18375	0.77 ± 0.19	⋯	⋯	0.38 ± 0.28	⋯	⋯	⋯	−1.30 ± 0.34	−1.43 ± 0.11
GAMA-628	0.45 ± 0.10	0.58 ± 0.08	0.13 ± 0.05	−0.01 ± 0.19	2.95 ± 0.14	2.63 ± 0.13	2.73 ± 0.13	−0.83 ± 0.26	−1.08 ± 0.05
GAMA-7807	0.54 ± 0.06	0.70 ± 0.06	0.16 ± 0.06	0.10 ± 0.17	3.51 ± 0.31	3.54 ± 0.41	3.47 ± 0.44	−1.12 ± 0.26	−1.45 ± 0.09
VAGC-96050	0.47 ± 0.05	0.58 ± 0.09	0.11 ± 0.08	0.02 ± 0.16	2.64 ± 0.41	3.04 ± 0.30	1.37 ± 0.61	−0.38 ± 0.24	−0.47 ± 0.05
Galaxies without stellar halo detection									
VAGC-411901	⋯	⋯	⋯	⋯	⋯	⋯	⋯	$\leqslant -1.66$	$\leqslant -1.60$
VAGC-527160	⋯	⋯	⋯	⋯	⋯	⋯	⋯	$\leqslant -2.01$	$\leqslant -1.91$
VAGC-57421	⋯	⋯	⋯	⋯	⋯	⋯	⋯	$\leqslant -2.08$	$\leqslant -1.92$
VAGC-166177	⋯	⋯	⋯	⋯	⋯	⋯	⋯	$\leqslant -1.55$	$\leqslant -1.75$
VAGC-57424	⋯	⋯	⋯	⋯	⋯	⋯	⋯	$\leqslant -1.84$	$\leqslant -2.02$
VAGC-60459	⋯	⋯	⋯	⋯	⋯	⋯	⋯	$\leqslant -1.43$	$\leqslant -1.55$

Note. This table presents the stellar halo properties of our high-inclination central galaxies, grouped according to whether a stellar halo is detected and sorted by the galaxy stellar mass. Columns: (1) galaxy name; (2) outer $g-r$ color; (3) outer $g-i$ color; (4) outer $r-i$ color; (5) outer mass-to-light ratio; (6) power-law index in the g band; (7) power-law index in the r band; (8) power-law index in the i band; (9) stellar halo mass fraction; (10) stellar halo flux fraction. All properties are measured in imaging data corrected for PSF-induced scatter light. All colors, mass-to-light ratio and mass are K-corrected and Galactic-extinction-corrected. The uncertainties represent the 1σ confidence level.

(This table is available in its entirety in machine-readable form in the online article.)

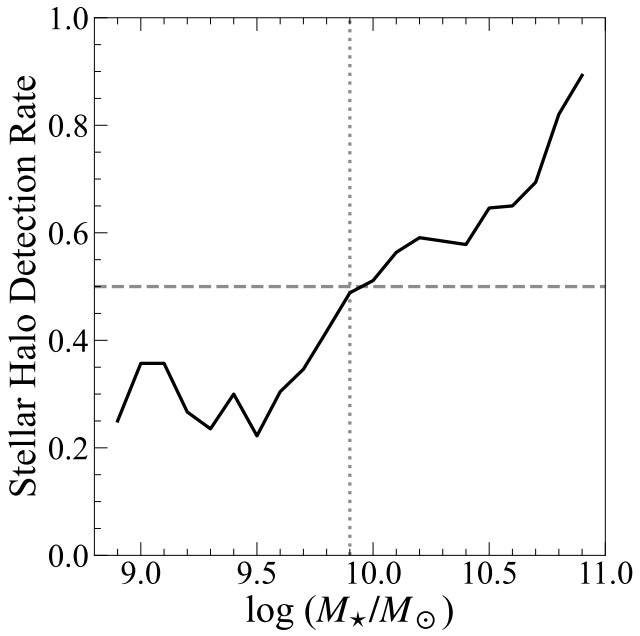

Figure 10. Stellar halo detection rate as a function of galaxy stellar mass. The halo detection rate falls well below 50% at $\log(M_\star/M_\odot) < 9.9$. See Section 4.1 for details.

4.4. Inner Boundary of the Stellar Halo-dominated Region

With a large sample of stellar halo detections in disk galaxies, it is helpful to examine the typical division radii between disk-dominated and halo-dominated regions. In addition to the standard definition of inner boundaries described in Section 3.3.2, referred to as $\mathrm{SMB}_{0,\mathrm{SH}}$, here we also show inner boundary radii where the halo ellipticity first reaches 0.5 (Section 3.3.1), referred to as $\mathrm{SMB}_{e=0.5,\mathrm{SH}}$. Figure 13 presents the distributions of $\mathrm{SMB}_{0,\mathrm{SH}}$ in units of kiloparsecs (panel (a)) and $R_{e,maj}$ (panel (b)), as well as $\mathrm{SMB}_{e=0.5,\mathrm{SH}}$ in units of kiloparsecs (panel (c)) and $R_{e,maj}$ (panel (d)). The effective radius $R_{e,maj}$ is the semimajor axis radius of the isophote containing half of the total flux in the r band for each galaxy.

In the left panels of Figure 13, the inner boundary measured in kiloparsecs shows a clear positive dependence on galaxy stellar mass, albeit with considerable overlap. The median values of $\mathrm{SMB}_{0,\mathrm{SH}}$ and $\mathrm{SMB}_{e=0.5,\mathrm{SH}}$ are $9.5^{+3.9}_{-2.9}$ kpc and $13.5^{+6.3}_{-2.7}$ kpc for the high-mass subsample, whereas they are $6.8^{+1.4}_{-2.1}$ kpc and $8.2^{+3.6}_{-2.1}$ kpc, respectively, for the low-mass subsample.

In contrast, when expressed in units of $R_{e,maj}$, the inner boundaries show virtually no dependence on galaxy mass. The median $\mathrm{SMB}_{0,\mathrm{SH}}$ and $\mathrm{SMB}_{e=0.5,\mathrm{SH}}$ are $1.5^{+1.2}_{-0.4}\,R_{e,maj}$ and $2.1^{+1.9}_{-0.4}\,R_{e,maj}$ for the high-mass subsample, very close to $1.4^{+0.8}_{-0.5}\,R_{e,maj}$ and $2.0^{+0.9}_{-0.5}\,R_{e,maj}$ for the low-mass subsample. The corresponding median values for the full sample are $1.5^{+0.7}_{-0.5}\,R_{e,maj}$ and $2.0^{+1.2}_{-0.5}\,R_{e,maj}$, respectively.

These results suggest that a fixed inner boundary in kiloparsecs cannot be used to measure stellar halos across a wide stellar mass range. Instead, a fixed minor-axis radius of $\sim$1.5–2.0$R_{e,maj}$, corresponding to $\sim$3–4$R_{e,maj}$ along the major axis for an axis ratio of 0.5, provides a more reasonable choice for statistical studies of large samples of high-inclination galaxies. Despite the constant median values in units of $R_{e,maj}$, the distribution of inner boundaries has a tail extending to $\sim 6R_{e,maj}$. Our results justify the conservative choice of C. Gilhuly et al. (2022), who adopted 5 times the half-mass–radius along the major axis to identify stellar halos.

4.5. Stellar Halo Color–Mass Relations

Figure 14 presents the integrated colors, $(g-r)_{\mathrm{halo}}$ and $(g-i)_{\mathrm{halo}}$ of the stellar halos as a function of the stellar halo mass for our sample. Nine galaxies with color uncertainties larger than 0.33 mag are not plotted. As is shown, the stellar halo colors have a moderate ($\rho \sim 0.3$–0.5) yet significant (p-values < 0.05) correlation with the mass.

Quiescent galaxies follow a tight color–magnitude or color–mass relation (commonly referred to as the red sequence), which is primarily driven by the correlation between metallicity and galaxy mass, whereas stellar age shows a weaker dependence on luminosity or stellar mass and mainly contributes to the color scatter at fixed mass (e.g., G. J. Graves et al. 2009). Since stellar halos generally consist of old stellar populations (e.g., A. Bressan et al. 1996; D. Carollo et al. 2016), the observed stellar halo color–mass correlation is likely mainly driven by a stellar halo mass–metallicity relation.

A. Smercina et al. (2022) observed a stellar halo mass–metallicity relation for 14 MW-mass galaxies in the Local Volume. To enable a direct comparison with our measurements, we convert the A. Smercina et al. (2022) mass–metallicity relation into color–mass relations using empirical color–metallicity correlations. Specifically, we derive a relation between color and metallicity by combining the galaxy stellar mass–metallicity relations from the local Universe (A. Gallazzi et al. 2005; E. N. Kirby et al. 2013) with the stellar mass–color relation of local elliptical galaxies (R. Chang et al. 2006).[13] The resulting stellar halo $(g-r)$–mass and $(g-i)$–mass relations for the 14 MW-mass galaxies are overplotted as dashed lines in Figure 14. The inferred $(g-r)$–mass relation agrees well with our measurements, whereas the inferred $(g-i)$–mass relation shows a slight systematic offset. The slight offset for $(g-i)$–mass relation may be explained by its higher sensitivity to stellar ages.

The presence of a stellar halo color–mass correlation, and its overall consistency with that inferred from the mass–metallicity relation, confirms the existence of a general halo mass–metallicity correlation. This correlation implies that stellar halos are predominantly built from the remnants of one or a few massive satellites, rather than from the accretion of numerous low-mass ones. This interpretation is consistent with theoretical expectations (e.g., R. D'Souza & E. F. Bell 2018a; A. Monachesi et al. 2019).

4.6. Stellar Halo Fraction

4.6.1. The Galaxy Mass Dependence for Our Sample

The flux or mass fraction of stellar halos relative to the total stellar mass of a galaxy reflects the cumulative contribution of merger events in the past. In the upper panels of Figure 15, we present the dependence of stellar halo mass and r-band flux fractions on galaxy stellar mass.

To explore the dependence of stellar halo fractions on galaxy stellar mass, it is necessary to account for both galaxies

[13] We apply K-corrections to the stellar color–mass relations reported in the paper, shifting them to $z = 0$.

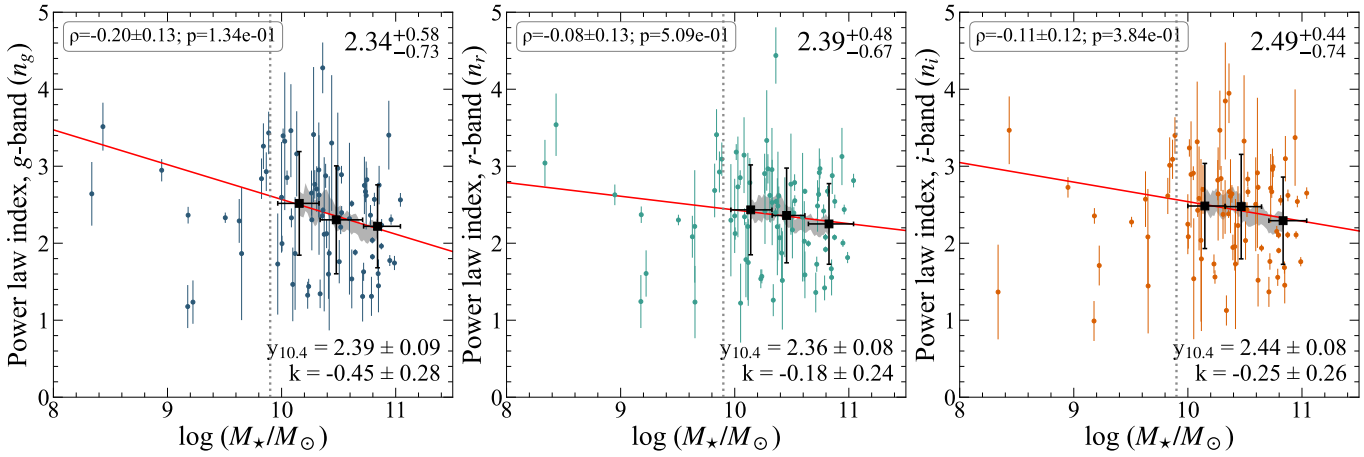

Figure 11. Power-law indices of stellar halo profiles are plotted against the host galaxy stellar mass. Results for the g-band profiles, r-band profiles, and i-band profiles are, respectively, shown in the left, middle, and right panels. The median and central 68% range of the indices for galaxies with $\log M_\star/M_\odot > 9.9$ (vertical gray dotted lines) are listed in the upper-right corners. The Spearman rank correlation coefficients, their uncertainties, and the p-values are listed in the upper-left corners. Running means and the rms scatters are shown as the gray shaded region. Large black squares with error bars indicate the mean and central 68% scatter of galaxies in three nonoverlapping galaxy mass intervals. The best-fit slope (k) and intercept at $\log M_\star/M_\odot = 10.4$ ($y_{10.4}$) are also provided, where $n = k \times (\log M_\star - 10.4) + y_{10.4}$, and 10.4 is the median logarithmic stellar mass of galaxies with halo detection. See Section 4.2 for details.

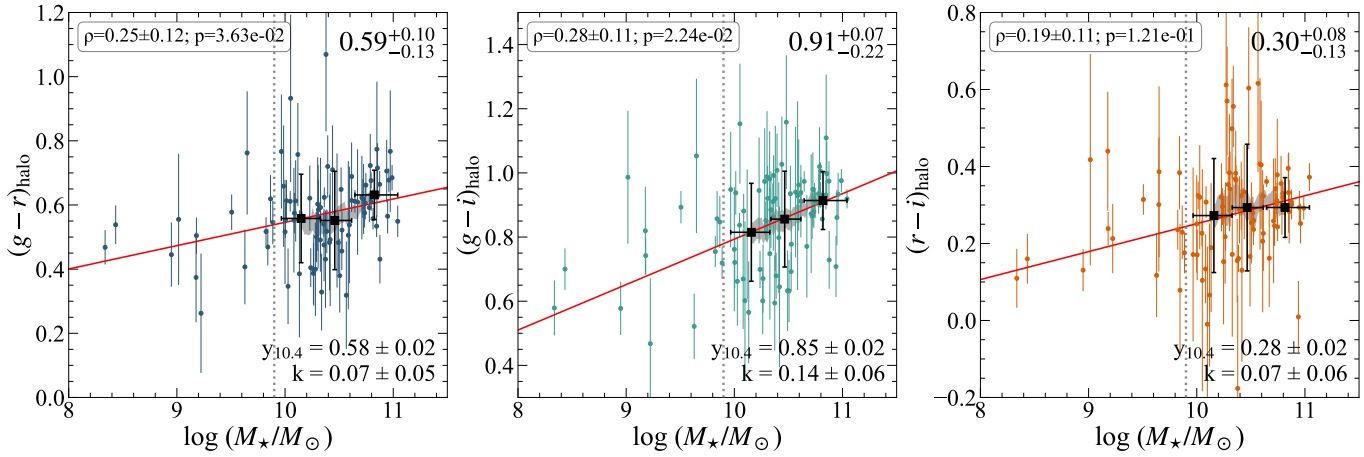

Figure 12. Similar to Figure 11, but showing the results of stellar halo colors of our galaxies. See Section 4.3 for details.

with and without stellar halo detections. We therefore estimate upper limits on the stellar halo fractions for galaxies without detected halos. Given that such galaxies are dominated by disk light out to the surface brightness limit of $\simeq$30 mag arcsec^{-2}, the stellar halo component is expected to contribute no more than half of the observed stellar light at this surface brightness level. This corresponds to a maximum stellar halo surface brightness of 30.75 mag arcsec^{-2} at the outermost galactocentric radii where galaxy light is detected.

The above upper limit, together with the galaxy-mass-dependent median power-law indices and mass-to-light ratios derived from galaxies with halo detections, allows us to place an upper limit on the total stellar halo mass for galaxies without detections. With both detections and upper limits included for the full sample, we employ two different methods to estimate the dependence of stellar halo fraction on galaxy stellar mass. The first method is the Kaplan–Meier (K-M) estimator, a commonly used survival analysis technique in astronomy for estimating median or mean values for datasets that include nondetections (e.g., A. R. Calette et al. 2018). The second method is the Bayesian linear regression approach `LINMIX` (B. C. Kelly 2007), which performs linear regression while explicitly accounting for nondetections.

The median stellar halo fractions and their 68th percentile confidence intervals, derived from the K-M estimator over 0.5 dex running windows in galaxy stellar mass, together with the maximum-likelihood linear relation obtained from `LINMIX`, are overplotted in the upper panels of Figure 15. The most likely `LINMIX` slope and intercept are also listed in each panel. We note that the `LINMIX` linear regression is restricted to galaxies with $\log(M_\star/M_\odot) > 10.2$, above which the K-M estimator yields a virtually log−log linear relationship (see the red shaded regions in Figure 15). Reassuringly, the two methods yield highly consistent median trend for the dependence of stellar halo fraction on galaxy stellar mass.

The median stellar halo flux fraction decreases monotonically with decreasing galaxy mass above the 50% detection rate limit, albeit with a larger uncertainty at $\log(M_\star/M_\odot) \lesssim 10.3$ (where detection rate is $\lesssim$60%). At

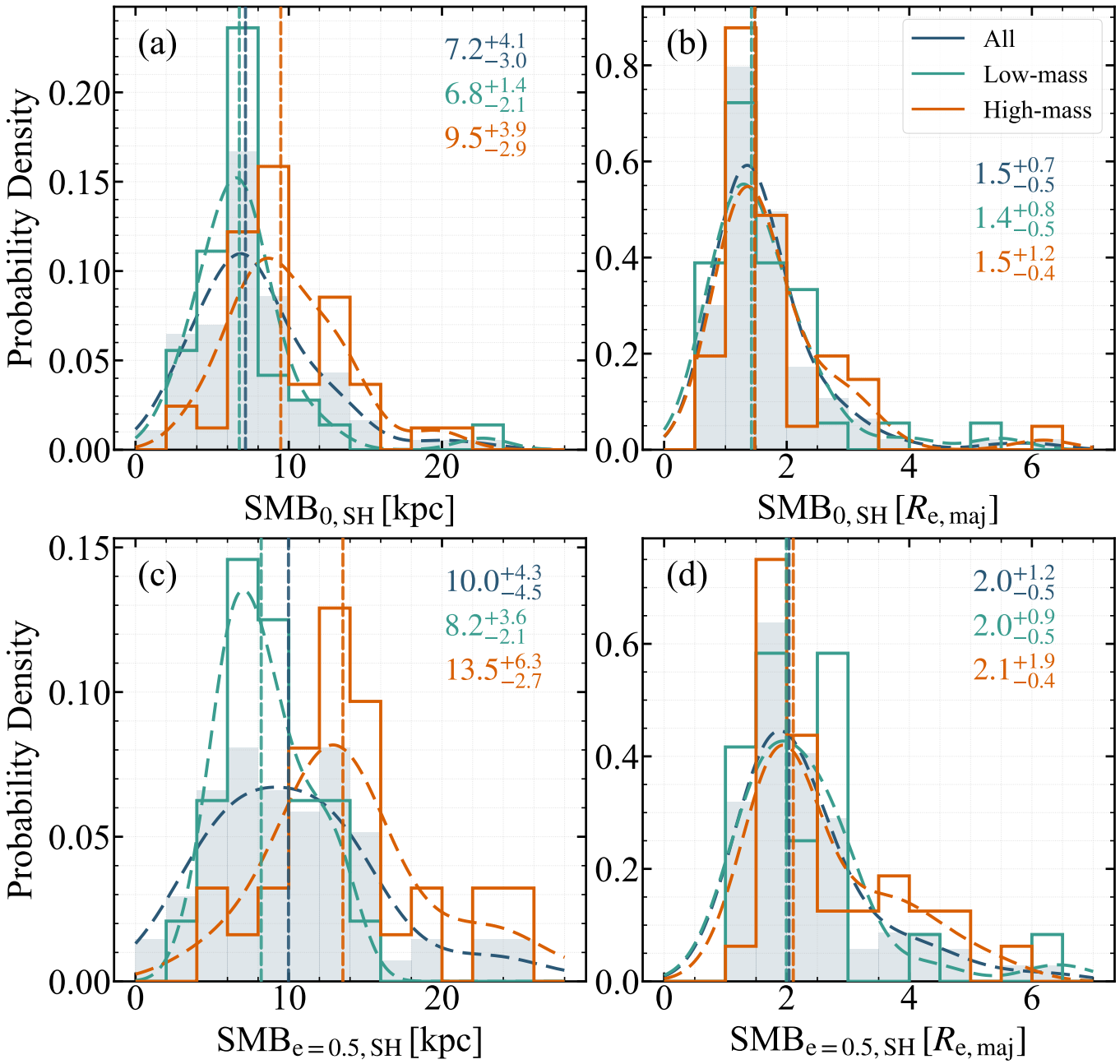

Figure 13. Distribution of the inner boundary of the stellar-halo-dominated region of our galaxies. The boundary is defined as the SMB radius, where stellar halo starts dominating over galaxy disk ($\mathrm{SMB}_{0,\mathrm{SH}}$; see Figure 8).The boundary is expressed in units of kiloparsecs (panel (a)) or $R_{\mathrm{e,maj}}$ (panel (b)). The distribution for the most prominent stellar halos with ellipticity <0.5 ($\mathrm{SMB}_{\mathrm{e=0.5,SH}}$) is shown in units of kiloparsecs (panel (c)) or $R_{\mathrm{e,maj}}$ (panel (d)). The sample is divided into low- and high-mass subsamples at a stellar mass of $10^{10.4}\,M_{\odot}$. Colored vertical dashed lines indicate the median values of each subsample. The median and central 68% range of the indices for the full sample, low- and high-mass subsamples are given in each panel. Colored dashed curves show the corresponding kernel density estimation profiles for each distribution, following the same color scheme as the histograms. See Section 4.4 for details.

$\log(M_{\star}/M_{\odot}) < 10.2$, all galaxies exhibit stellar halo fractions higher than that expected from the linear extrapolation of the relation at higher masses (red dashed lines in the upper panels of Figure 15), with no clear dependence on galaxy mass for either detections or upper limits. This flattening trend at the low-mass end likely reflects a detection bias due to the low detection rate, but may also partly indicate an intrinsically weak mass dependence, as predicted by cosmological simulations (e.g., V. Rodriguez-Gomez et al. 2016; R. Shi et al. 2022).

To be quantitative, there is a strong correlation ($\rho \sim 0.44$) between the halo mass fraction and the galaxy stellar masses at $\log M_{\star}/M_{\odot} > 10.3$. The correlation coefficient for stellar halo flux fraction is slightly lower ($\rho \sim 0.39$).

The lower-left panel of Figure 15 shows the histogram of the stellar halo mass fraction for MW-mass galaxies with $10.5 < \log(M_{\star}) < 11.0$. The K-M estimator median stellar halo mass fraction (in logarithm) for this subsample is -1.0 dex (with a $+0.2/-0.3$ dex uncertainty considering the 95% confidence intervals), $\sim$ 0.1 dex lower than the median for galaxies with halo detections. There is a substantial spread in the halo fractions, with the 5th–95th percentiles spanning -1.5 to -0.5 dex for galaxies with detected halos, indicating diverse merger histories. We note that our results for MW-

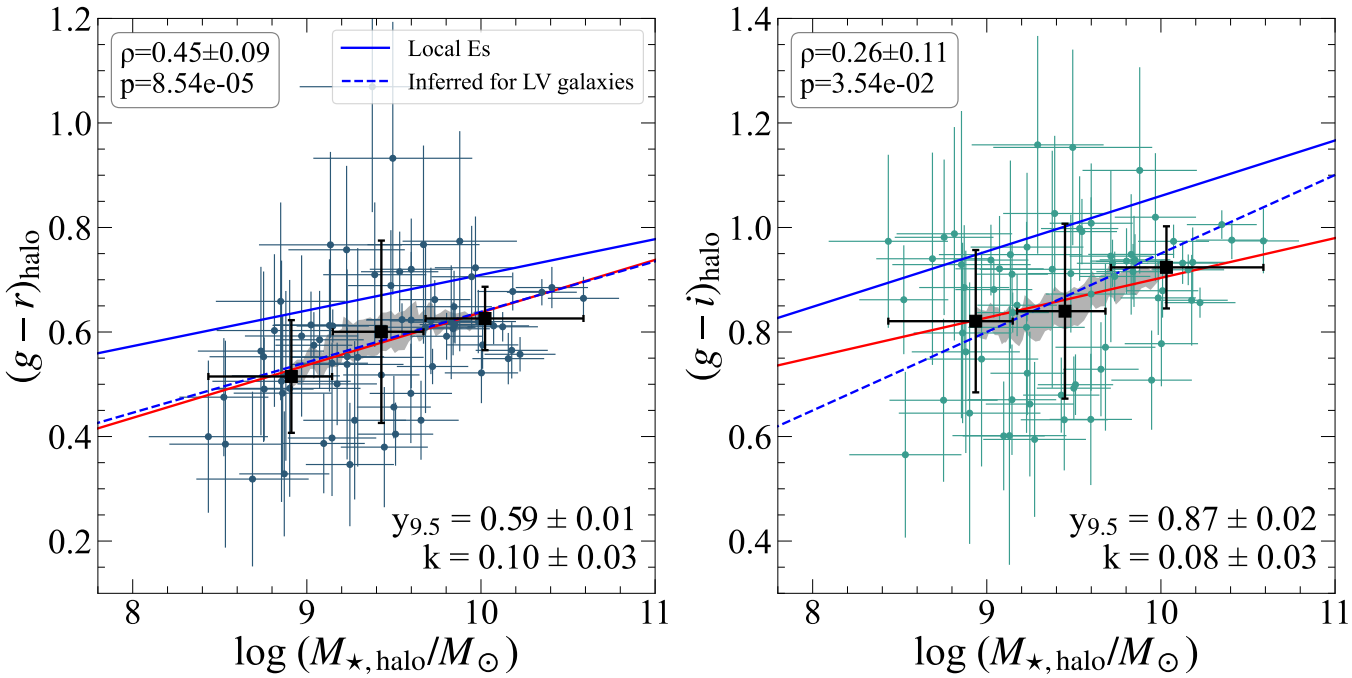

Figure 14. Stellar halo colors are plotted against stellar halo masses for our galaxies. Results for the $(g-r)_{\rm halo}$ and $(g-i)_{\rm halo}$ are, respectively, shown in the left and right panels. The blue solid lines show the color–mass relation of local elliptical galaxies, while the blue dashed lines represent the relation inferred from the halo mass–metallicity correlation of the stellar halos of 14 Local Volume MW-mass galaxies (A. Smercina et al. 2022). The Spearman rank correlation coefficients, their uncertainties, and the p-values are listed in the upper-left corners. Running average and the rms scatter are shown as the gray shaded region. Large black squares with error bars indicate the average and central 68% scatter of galaxies in three separate galaxy mass intervals. The best-fit linear relations (color $= k \times (\log M_\star - 9.5) + y_{9.5}$) for our sample are shown as red lines, and the best-fit slope (k) and intercept at $\log M_\star/M_\odot = 9.5$ ($y_{9.5}$) are also provided. See Section 4.5 for details.

mass galaxies in this paper are virtually identical when stellar halos are measured over a fixed minor-axis radial range of 10–40 kpc, rather than a normalized radial range.

4.6.2. Comparison with MW and Other Nearby Galaxies

With the first highly complete stellar halo detections for disk galaxies at $\log(M_\star) \gtrsim 10.0$, we can assess how representative familiar systems such as the MW and M31 are in terms of their stellar halo fractions.

The most up-to-date estimate of the logarithmic stellar halo mass fraction of the MW is -1.64 ± 0.15 for a Kroupa IMF (A. J. Deason et al. 2019), about 0.43 dex larger than the value reported earlier by B. Harmsen et al. (2017). As shown in Figure 15, the MW's stellar halo mass fraction is ∼0.6 dex lower than the typical value for galaxies of similar mass, suggesting an unusually quiescent merger history. We note that a relatively quiet merger history for the MW has been inferred by several recent studies (G. R. Ruchti et al. 2015; F. Fragkoudi et al. 2020; A. J. Deason et al. 2023). In contrast to the MW, the stellar halo mass fraction of M31 (-0.71 ± 0.30 dex; J. Sick et al. 2015; R. D'Souza et al. 2018b; A. Smercina et al. 2022) follows the median halo fraction–galaxy mass relation.

The largest samples of stellar halo measurements of nearby galaxies were presented by A. Smercina et al. (2022) and C. Gilhuly et al. (2022). Together, the two studies include 17 unique extragalactic MW-mass galaxies ($10.5 < \log M_\star/M_\odot < 11.0$) within 25 Mpc. For the galaxies NGC 4565 and M101, which are common to both studies, we adopt the halo measurement from A. Smercina et al. (2022). A. Smercina et al. (2022) measured stellar halo mass as 3 times the mass enclosed within a mino r-axis radial range of 10–40 kpc, whereas C. Gilhuly et al. (2022) reported halo fractions measured beyond 20 kpc along the major axis, which is approximately equivalent to a minor-axis radius of 10 kpc (see C. Gilhuly et al. 2022, for a comparison). We note that the surface brightness profiles of eight galaxies studied by C. Gilhuly et al. (2022) have outer minor-axis radial boundaries of <30 kpc, which fall well short of the 40 kpc requirement. These eight galaxies are therefore excluded from our comparison. After applying the same multiplicative factor of 3 to the C. Gilhuly et al. (2022) measurements for consistency, the resulting halo fractions for all 17 galaxies are overplotted in the upper panels of Figure 15.

Interestingly, 68% (13/19) of the nearby galaxies, including the MW and M31, lie below the median relation defined by our sample (upper panels of Figure 15), and this fraction is 72% when considering only the 11 Local Volume galaxies. The median stellar halo fraction of these nearby galaxies (−1.30 dex, or −1.55 dex when considering only Local Volume galaxies) is ∼0.3 dex lower than the median value of our MW-mass galaxies (lower-left panel of Figure 15).

4.6.3. Dependence on Heliocentric Distance

In light of the significantly lower typical stellar halo fractions of nearby MW-mass galaxies found above, we explore potential systematic variations of the halo fractions with heliocentric distance. To this end, we divide our full MW-mass sample ($\log M_\star/M_\odot \geqslant 10.5$, including both detections and upper limits) into two halves at a redshift of 0.07 and compare these two redshift intervals with the nearby galaxy sample at distances <25 Mpc. We emphasize that the galaxy sample at $\log M_\star/M_\odot \geqslant 10.5$ is complete up to the redshift limit of 0.1 in our analysis (Figure 1), ensuring a meaningful

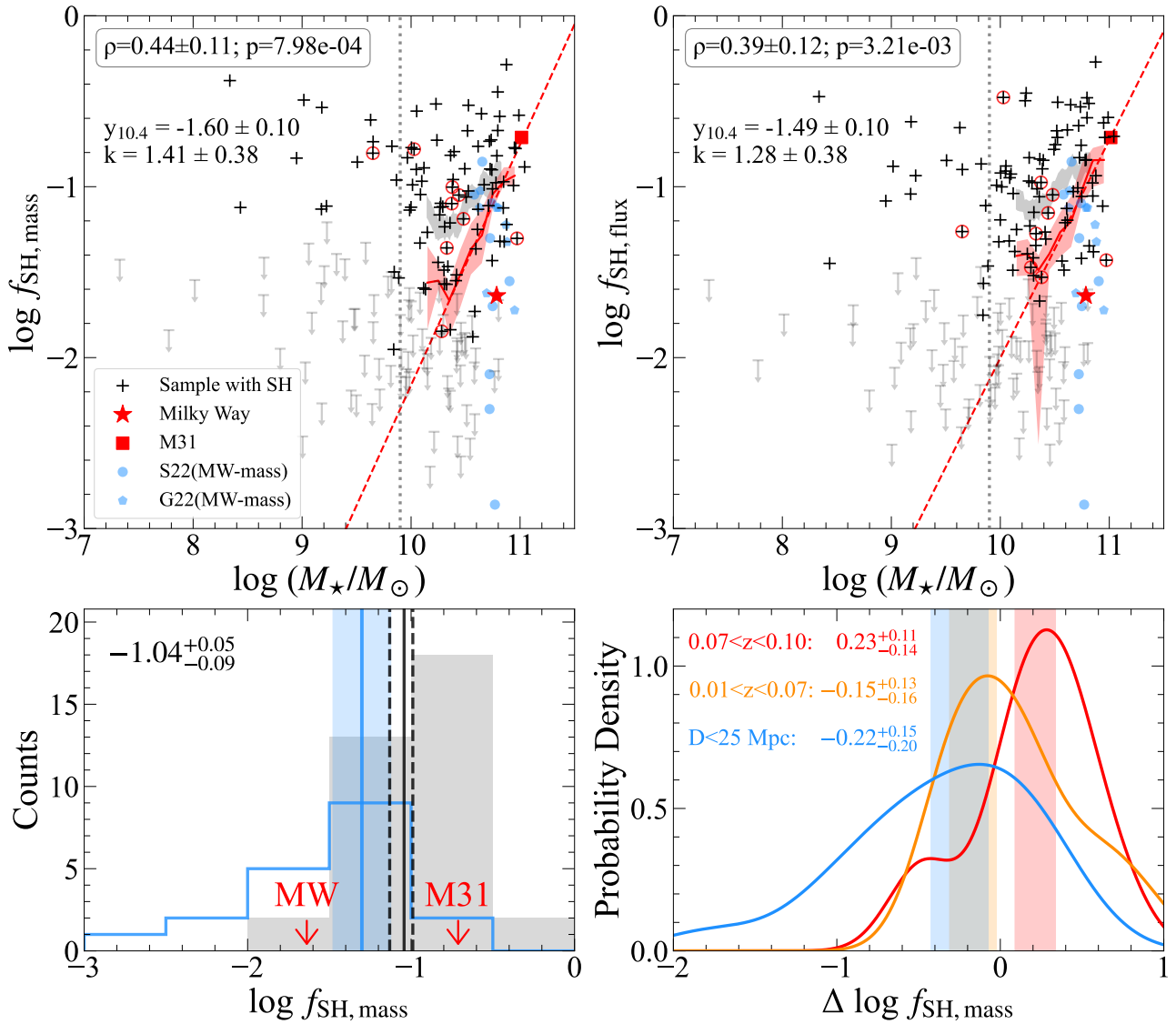

Figure 15. Stellar halo mass and flux fractions relative to host galaxies. Upper-left and -right panels: stellar halo mass/flux fraction vs. galaxy stellar mass. Black plus symbols denote galaxies with halo detections; those enclosed by red circles have power-law surface profiles and $q < 0.4$ in the outskirts. Gray arrows indicate upper limits for nondetections. The gray shaded region shows the rms scatter of mean fractions from 1000 bootstrap resamplings of detected halos in running stellar-mass bins. Literature measurements for the MW (red pentagram) and M31 (red square), and 17 nearby MW-mass galaxies ($10.5 < \log M_\star/M_\odot < 11.0$) within 25 Mpc from (A. Smercina et al. 2022, S22) and (C. Gilhuly et al. 2022, G22; blue), are included. Spearman coefficients, uncertainties, and p-values for detected halos at $\log M_\star/M_\odot > 10.3$ are listed. The red solid line and shaded region show the Kaplan–Meier (K-M) estimator median halo fractions and 1σ scatter over 0.5 dex running mass bins with 0.1 dex steps. Best-fit LINMIX relations for $\log M_\star/M_\odot \geqslant 10.2$, $\log f_{\rm SH} = k\,(\log M_\star - 10.4) + y_{10.4}$, are shown as red dashed lines, with k and $y_{10.4}$ listed. Lower-left panel: histograms of stellar halo mass fractions of MW-mass galaxies. Gray shaded and blue open histograms, respectively, represent galaxies from our sample and nearby galaxies within 25 Mpc. Vertical solid and dashed lines mark the median (based on K-M estimator for our sample) and the central 68% intervals. The blue shaded region represents the 68% confidence intervals from 1000 bootstrap resamplings of nearby galaxies. Lower-right panel: kernel density estimates of differential stellar halo fraction distributions for MW-mass galaxies within <25 Mpc and MW-mass galaxies below and above $z = 0.07$ in our sample. The differential halo mass fractions are derived by subtracting the median stellar halo mass fraction–galaxy mass relation from individual galaxies. Median values and 68% confidence intervals are shown by color-shaded regions and listed. See Section 4.6 for details.

comparative analysis of subsamples across different redshift intervals.

Because there is a significant halo fraction–galaxy mass correlation, we subtract (in logarithmic space) the halo fraction predicted by the median relation (the red dashed lines in the upper panels of Figure 15) from the measured value for each galaxy in the three samples introduced above. This subtraction is necessary to avoid potential biases introduced by differences in the galaxy mass distributions among the three samples. The resulting distributions of the differential halo fraction ($\Delta \log f_{\rm SH,mass}$) of the three samples are shown in the lower-right panel of Figure 15. We use kernel density estimates to represent the distributions. The median $\Delta \log f_{\rm SH,mass}$ and its 68% confidence interval are indicated as color-filled regions and listed in the upper-left corner of the panel. The values for our two samples are derived from the K-M estimator.

As shown, there is a systematic increase in the median halo fractions with heliocentric distance, although the difference between that of the nearby galaxies and our lower-redshift sample is not statistically significant. It is worth noting that the median stellar halo fraction of our $z > 0.07$ galaxies, i.e., $0.23 + (-1.04) = -0.81$ dex, where -1.04 is the K-M estimator median fraction of the full MW-mass sample (lower-left panel of Figure 15), is in good agreement with the median

accreted stellar fraction (−0.72 dex) of MW-mass galaxies in general in the TNG50 simulations (D. Sotillo-Ramos et al. 2022). This implies unusually quiescent merger histories for galaxies in the lower-redshift samples.

This unusually quiescent merger history of nearby galaxies appears consistent with earlier findings indicating that giant, nearly bulgeless disk galaxies are surprisingly more prevalent in the Local Volume than in rich clusters (e.g., J. Kormendy et al. 2010; J. Shen et al. 2010). It has been found that the local Universe out to redshift 0.07 (∼300 Mpc) is underdense relative to the large-scale cosmic average, with the matter density gradually increasing with distance within this volume, beyond which it remains more or less consistent with the cosmic average (e.g., R. C. Keenan et al. 2013; I. Banik & V. Kalaitzidis 2025). Together, these results help clarify the conundrum identified by the Dragonfly team (A. Merritt et al. 2020) for nearby galaxies, where typical stellar halo fractions appear lower than predicted by cosmological hydrodynamical simulations. These findings also align with W. Wang et al. (2021b), who reported that MW-mass galaxies within $\lesssim$40 Mpc exhibit an anomalous deficit of low-mass satellite galaxies relative to averages measured over larger scales.

5. Summary

We utilize deep imaging data from the Hyper Suprime-Cam Subaru Strategic Program Survey Public Data Release 3 (HSC-SSP PDR3) Deep/UltraDeep layers to investigate and characterize the stellar halo properties of 169 high-inclination central galaxies with stellar masses ranging from $10^{7.33}$ to $10^{11.04}M_{\odot}$. The central galaxy sample is constructed from the SDSS DR7 and GAMA DR4 spectroscopic surveys, selecting galaxies with r-band magnitudes brighter than 17.77 mag at $z < 0.1$. High-inclination systems are selected by requiring deconvolved disk axis ratios $q_{\rm disk} < 0.4$.

As dynamically hot structures, stellar halos are generally more spherical than disks. Our primary criterion for stellar halo identification (Section 3.3.2), applied to images corrected for PSF-induced scattered light, is based on isophotal ellipticity (or equivalently, axis ratios). This represents an improvement over previous approaches that relied on somewhat arbitrary galactocentric radii or multicomponent surface brightness decompositions without clear justification. Using this method, we detect stellar halos in 93 galaxies.

This is the first systematic census of stellar halos in a flux-limited, large sample of high-inclination central disk galaxies in the local Universe. The detection rate exceeds 50% for galaxies with stellar masses above $10^{9.9}M_{\odot}$ and rises to $\gtrsim$ 70% for MW-mass galaxies (Figure 10). This sample will be used to put unique constraints on the accretion histories of disk galaxies and their connection to other galaxy properties in an accompanying paper. In the current paper, we provide the basic galaxy properties (Table 2) and derive the stellar halo measurements of the sample, including power-law surface brightness profile fitting, colors, halo mass, and fractions (Table 3). The main results of this work are as follows:

1. By analyzing a subsample of the 49 most prominent stellar halos (Section 3.3.1), we found that five of them are best described by an exponential radial decline in surface brightness and 44 by a single or broken power-law model. This result demonstrates that stellar halos generally follow power-law surface brightness profiles.
2. The power-law indices n of stellar halo surface brightness profiles exhibit weak but systematic variation from the g to i band, with the redder bands having larger median n and thus steeper radial decline, implying negative color gradients of stellar halos. In addition, more-massive galaxies have lower median n values, indicating their more extended stellar halo profiles (Section 4.2).
3. The optical colors of the stellar halos exhibit a positive dependence on stellar mass of the host galaxies, with more-massive galaxies having redder median colors (Section 4.3). The redder colors likely arise from a generally higher metallicity of stellar halos in more-massive galaxies.
4. The inner radial boundary, where stellar halos begin to dominate over stellar disks at larger minor-axis radii, shows a significant positive dependence on galaxy stellar mass when expressed in kiloparsecs. However, this systematic dependence largely disappears when the inner boundaries are normalized by the major-axis half-light radius $R_{\rm e,maj}$, yielding a nearly constant median value of $\sim$1.5–2.0$R_{\rm e,maj}$ (depending on the exact definition) along the minor axis (Section 4.4).
5. The optical colors of stellar halos show a moderately strong positive correlation with stellar halo mass. This correlation primarily reflects an underlying stellar halo mass–metallicity relation, indicating that stellar halos are largely built from the remnants of a few massive (rather than numerous very low-mass) merger events, consistent with cosmological simulations.
6. There exists a significant positive correlation between stellar halo fractions and galaxy stellar mass for galaxies with $\log(M_{\star}/M_{\odot}) \gtrsim 10.0$, where the halo detection rate is relatively high (Figure 15). This is consistent with theoretical expectations that more-massive galaxies generally experienced more active merger histories.
7. Our MW has a stellar halo fraction ∼0.6 dex below the median stellar halo fraction–galaxy mass relation. Comparing the stellar halo fraction distributions of nearby galaxies within 25 Mpc with those of the lower-redshift ($z < 0.07$) and higher-redshift galaxies in our sample indicates a systematic increase in typical halo fraction with heliocentric distance, with the galaxies at $z > 0.07$ showing median values in good agreement with IllustrisTNG predictions. The unusually quiescent merger histories implied for nearby galaxies appear to align with the underdense nature of the local Universe out to $z \lesssim 0.07$ (Section 4.6.3).

Acknowledgments

This work has been supported by the National Key Research and Development Program of China (No. 2023YFA1608100), the NSFC (Nos. 12122303, 11973039), and the China Manned Space Program with grant Nos. CMS-CSST-2021-B02, CMS-CSST-2025-A08 and CMS-CSST-2021-A07. We also acknowledge support from the CAS Pioneer Hundred Talents Program, and the Cyrus Chun Ying Tang Foundations. H.Y.W. is supported by the National Natural Science Foundation of China (NSFC, No. 12192224) and CAS Project for Young Scientists in Basic Research, grant No. YSBR-062. G.C. acknowledges support provided by the Spanish Ministerio de Ciencia, Innovación y Universidades (MICIU) through the project PID2023-153342NB-I00 / 10.13039/501100011033.

The Hyper Suprime-Cam (HSC) collaboration includes the astronomical communities of Japan and Taiwan, and Princeton University. The HSC instrumentation and software were developed by the National Astronomical Observatory of Japan (NAOJ), the Kavli Institute for the Physics and Mathematics of the Universe (Kavli IPMU), the University of Tokyo, the High Energy Accelerator Research Organization (KEK), the Academia Sinica Institute for Astronomy and Astrophysics in Taiwan (ASIAA), and Princeton University. Funding was contributed by the FIRST program from the Japanese Cabinet Office, the Ministry of Education, Culture, Sports, Science and Technology (MEXT), the Japan Society for the Promotion of Science (JSPS), Japan Science and Technology Agency (JST), the Toray Science Foundation, NAOJ, Kavli IPMU, KEK, ASIAA, and Princeton University.

This work is based in part on data collected at the Subaru Telescope and retrieved from the HSC data archive system, which is operated by Subaru Telescope and Astronomy Data Center at National Astronomical Observatory of Japan.

Appendix
Estimate of Local Background and Its Noise

We define a series of concentric annular regions centered on each of our sample galaxies, with the radius ratio between adjacent annulus set to 1.1. The intensity of each annulus is defined as the median of unmasked pixels within the annulus. The background region is defined as the first occurrence of six contiguous annuli where the radial intensity gradient is close to zero. We then divided the background region into 24 quadrants along the major and minor axes of these central galaxies and utilized the `sigma_clipped_stats` function to measure the 5σ clipped median ($I_{\rm sky,i}$) and standard deviation ($\sigma_{\rm sky,i}$) of unmasked pixels in the ith quadrant. The local background value was set as the median of $I_{\rm sky,i}$. The high-frequency background noise $\Delta I_{\rm sky,high}$ was calculated as the median of $\sigma_{\rm sky,i}/\sqrt{N_{\rm sky,i}}$, where $N_{\rm sky,i}$ indicates the number of unmasked pixels in a given quadrant. The low-frequency background noise $\Delta I_{\rm sky,low}$ was calculated by combining the standard deviation of the $I_{\rm sky,i}$ and the high-frequency background noise; see A. Gil de Paz & B. F. Madore (2005) for details. In addition to the background noise $\Delta I_{\rm sky}$, the uncertainty of the median background value is derived as $\Delta I_{sky}/\sqrt{24}$. By doing the above, we obtained an estimate of local depth of surface photometry for each galaxy as $2 \times \Delta I_{\rm sky}$.

ORCID iDs

Bojun Tao https://orcid.org/0000-0002-8420-6246
Hong-Xin Zhang https://orcid.org/0000-0003-1632-2541
Wenting Wang https://orcid.org/0000-0002-5762-7571
Enci Wang https://orcid.org/0000-0003-1588-9394
Guangwen Chen https://orcid.org/0000-0002-4742-8800
Huiyuan Wang https://orcid.org/0000-0002-4911-6990
Qian-Hui Chen https://orcid.org/0000-0002-4382-1090
Song Huang https://orcid.org/0000-0003-1385-7591
Xu Kong https://orcid.org/0000-0002-7660-2273
Yu Rong https://orcid.org/0000-0002-2204-6558

References

Ablimit, I., & Zhao, G. 2018, ApJ, 855, 126
Ablimit, I., Zhao, G., Teklimakan, U., Shi, J.-R., & Abdusalam, K. 2022, ApJS, 258, 20
Aihara, H., Arimoto, N., Armstrong, R., et al. 2018, PASJ, 70, S4
Aihara, H., AlSayyad, Y., Ando, M., et al. 2022, PASJ, 74, 247
An, D., Beers, T. C., Johnson, J. A., et al. 2013, ApJ, 763, 65
Angeloudi, E., Falcón-Barroso, J., Huertas-Company, M., et al. 2024, NatAs, 8, 1310
Banik, I., & Kalaitzidis, V. 2025, MNRAS, 540, 545
Bell, E. F., Monachesi, A., Harmsen, B., et al. 2017, ApJL, 837, L8
Bell, E. F., Zucker, D. B., Belokurov, V., et al. 2008, ApJ, 680, 295
Belokurov, V., Erkal, D., Evans, N. W., Koposov, S. E., & Deason, A. J. 2018, MNRAS, 478, 611
Bernardi, M., Meert, A., Sheth, R. K., et al. 2013, MNRAS, 436, 697
Blanton, M. R., Schlegel, D. J., Strauss, M. A., et al. 2005, AJ, 129, 2562
Bressan, A., Chiosi, C., & Tantalo, R. 1996, A&A, 311, 425
Bullock, J. S., & Johnston, K. V. 2005, ApJ, 635, 931
Calette, A. R., Avila-Reese, V., Rodríguez-Puebla, A., Hernández-Toledo, H., & Papastergis, E. 2018, RMxAA, 54, 443
Carney, B. W., & Latham, D. W. 1986, AJ, 92, 60
Carollo, D., Beers, T. C., Chiba, M., et al. 2010, ApJ, 712, 692
Carollo, D., Beers, T. C., Placco, V. M., et al. 2016, NatPh, 12, 1170
Chang, R., Gallazzi, A., Kauffmann, G., et al. 2006, MNRAS, 366, 717
Chen, A., Li, Z., Wang, Y., et al. 2023, MNRAS, 525, 3075
Chiba, M., & Beers, T. C. 2000, AJ, 119, 2843
Chilingarian, I. V., Melchior, A.-L., & Zolotukhin, I. Y. 2010, MNRAS, 405, 1409
Cohen, R. E., Goudfrooij, P., Correnti, M., et al. 2020, ApJ, 890, 52
Cooper, A. P., D'Souza, R., Kauffmann, G., et al. 2013, MNRAS, 434, 3348
Cooper, A. P., Frenk, C. S., Hellwing, W. A., & Bose, S. 2025, MNRAS,
Cooper, A. P., Gao, L., Guo, Q., et al. 2015, MNRAS, 451, 2703
Cooper, A. P., Cole, S., Frenk, C. S., et al. 2010, MNRAS, 406, 744
Das, P., Williams, A., & Binney, J. 2016, MNRAS, 463, 3169
de Jong, R. S. 2008, MNRAS, 388, 1521
Deason, A. J., & Belokurov, V. 2024, NewAR, 99, 101706
Deason, A. J., Belokurov, V., & Evans, N. W. 2011, MNRAS, 416, 2903
Deason, A. J., Belokurov, V., Evans, N. W., & Johnston, K. V. 2013, ApJ, 763, 113
Deason, A. J., Belokurov, V., & Sanders, J. L. 2019, MNRAS, 490, 3426
Deason, A. J., Koposov, S. E., Fattahi, A., & Grand, R. J. J. 2023, MNRAS, 520, 6091
Driver, S. P., Bellstedt, S., Robotham, A. S. G., et al. 2022, MNRAS, 513, 439
D'Souza, R., & Bell, E. F. 2018a, MNRAS, 474, 5300
D'Souza, R., & Bell, E. F. 2018b, NatAs, 2, 737
D'Souza, R., Kauffman, G., Wang, J., & Vegetti, S. 2014, MNRAS, 443, 1433
D'Souza, R., Vegetti, S., & Kauffmann, G. 2015, MNRAS, 454, 4027
Eggen, O. J., Lynden-Bell, D., & Sandage, A. R. 1962, ApJ, 136, 748
Elias, L. M., Sales, L. V., Creasey, P., et al. 2018, MNRAS, 479, 4004
Favaro, J., Courteau, S., Comerón, S., & Stone, C. 2025, ApJ, 978, 63
Fernández-Alvar, E., Carigi, L., Allende Prieto, C., et al. 2017, MNRAS, 465, 1586
Font, A. S., Benson, A. J., Bower, R. G., et al. 2011, MNRAS, 417, 1260
Fragkoudi, F., Grand, R. J. J., Pakmor, R., et al. 2020, MNRAS, 494, 5936
Gaia Collaboration, Prusti, T., de Bruijne, J., H., J., et al. 2016, A&A, 595, A1
Gaia Collaboration, Brown, A. G. A., Vallenari, A., et al. 2021, A&A, 649, A1
Gallazzi, A., Charlot, S., Brinchmann, J., White, S. D. M., & Tremonti, C. A. 2005, MNRAS, 362, 41
Genina, A., Deason, A. J., & Frenk, C. S. 2023, MNRAS, 520, 3767
Gil de Paz, A., & Madore, B. F. 2005, ApJS, 156, 345
Gilhuly, C., Merritt, A., Abraham, R., et al. 2022, ApJ, 932, 44
Gozman, K., Bell, E. F., Smercina, A., et al. 2023, ApJ, 947, 21
Graves, G. J., Faber, S. M., & Schiavon, R. P. 2009, ApJ, 693, 486
Greggio, L., Falomo, R., & Scarpa, R. 2018, ApJ, 861, 81
Grimozzi, S. E., Font, A. S., & De Rossi, M. E. 2024, MNRAS, 530, 95
Guo, Q., White, S., Li, C., & Boylan-Kolchin, M. 2010, MNRAS, 404, 1111
Hammer, F., Yang, Y. B., Wang, J. L., et al. 2018, MNRAS, 475, 2754
Harmsen, B., Bell, E. F., D'Souza, R., et al. 2023, MNRAS, 525, 4497
Harmsen, B., Monachesi, A., Bell, E. F., et al. 2017, MNRAS, 466, 1491
Harris, W. E. 1976, AJ, 81, 1095
Harris, W. E., & Canterna, R. 1979, ApJL, 231, L19
Hartwick, F. D. A. 1976, ApJ, 209, 418
Helmi, A. 2008, A&ARv, 15, 145
Helmi, A., Babusiaux, C., Koppelman, H. H., et al. 2018, Natur, 563, 85
Helmi, A., White, S. D. M., de Zeeuw, P. T., & Zhao, H. 1999, Natur, 402, 53
Ibata, R., Irwin, M., Lewis, G., Ferguson, A. M. N., & Tanvir, N. 2001, Natur, 412, 49
Ibata, R., Mouhcine, M., & Rejkuba, M. 2009, MNRAS, 395, 126
Ibata, R. A., Lewis, G. F., McConnachie, A. W., et al. 2014, ApJ, 780, 128
Infante-Sainz, R., Trujillo, I., & Román, J. 2020, MNRAS, 491, 5317

Iorio, G., Belokurov, V., Erkal, D., et al. 2018, MNRAS, 474, 2142
Jang, I. S., de Jong, R. S., Holwerda, B. W., et al. 2020, A&A, 637, A8
Jurić, M., Ivezić, Ž., Brooks, A., et al. 2008, ApJ, 673, 864
Karademir, G. S., Remus, R.-S., Burkert, A., et al. 2019, MNRAS, 487, 318
Kautsch, S. J., Grebel, E. K., Barazza, F. D., & Gallagher, J. S., III 2006, A&A, 445, 765
Keenan, R. C., Barger, A. J., & Cowie, L. L. 2013, ApJ, 775, 62
Keller, B. W. 2022, ApJ, 939, 4
Kelly, B. C. 2007, ApJ, 665, 1489
Kirby, E. N., Cohen, J. G., Guhathakurta, P., et al. 2013, ApJ, 779, 102
Kormendy, J., Drory, N., Bender, R., & Cornell, M. E. 2010, ApJ, 723, 54
Lackner, C. N., Cen, R., Ostriker, J. P., & Joung, M. R. 2012, MNRAS, 425, 641
Liu, Q., Abraham, R., Gilhuly, C., et al. 2022, ApJ, 925, 219
Mackereth, J. T., Schiavon, R. P., Pfeffer, J., et al. 2019, MNRAS, 482, 3426
McConnachie, A. W., Ibata, R., Martin, N., et al. 2018, ApJ, 868, 55
Medina, G. E., Muñoz, R. R., Carlin, J. L., et al. 2024, MNRAS, 531, 4762
Merritt, A., Pillepich, A., van Dokkum, P., et al. 2020, MNRAS, 495, 4570
Merritt, A., van Dokkum, P., Abraham, R., & Zhang, J. 2016, ApJ, 830, 62
Monachesi, A., Bell, E. F., Radburn-Smith, D. J., et al. 2016, MNRAS, 457, 1419
Monachesi, A., Gómez, F. A., Grand, R. J. J., et al. 2019, MNRAS, 485, 2589
Moore, B., Ghigna, S., Governato, F., et al. 1999, ApJL, 524, L19
Mouhcine, M., Ferguson, H. C., Rich, R. M., Brown, T. M., & Smith, T. E. 2005, ApJ, 633, 821
Mouhcine, M., Ibata, R., & Rejkuba, M. 2010, ApJL, 714, L12
Mouhcine, M., Rejkuba, M., & Ibata, R. 2007, MNRAS, 381, 873
Myeong, G. C., Vasiliev, E., Iorio, G., Evans, N. W., & Belokurov, V. 2019, MNRAS, 488, 1235
Naidu, R. P., Conroy, C., Bonaca, A., et al. 2020, ApJ, 901, 48
Oser, L., Ostriker, J. P., Naab, T., Johansson, P. H., & Burkert, A. 2010, ApJ, 725, 2312
Peacock, M. B., Strader, J., Romanowsky, A. J., & Brodie, J. P. 2015, ApJ, 800, 13
Peng, C. Y., Ho, L. C., Impey, C. D., & Rix, H.-W. 2002, AJ, 124, 266
Peng, C. Y., Ho, L. C., Impey, C. D., & Rix, H.-W. 2010, AJ, 139, 2097
Pila-Díez, B., de Jong, J. T. A., Kuijken, K., van der Burg, R. F. J., & Hoekstra, H. 2015, A&A, 579, A38
Pillepich, A., Vogelsberger, M., Deason, A., et al. 2014, MNRAS, 444, 237
Planck Collaboration, Ade, P. A. R., Aghanim, N., et al. 2014, A&A, 571, A16
Preston, G. W., Shectman, S. A., & Beers, T. C. 1991, ApJ, 375, 121
Racine, R. 1991, AJ, 101, 865
Reitzel, D. B., & Guhathakurta, P. 2002, AJ, 124, 234
Rejkuba, M., Harris, W. E., Greggio, L., Crnojević, D., & Harris, G. L. H. 2022, A&A, 657, A41
Rejkuba, M., Mouhcine, M., & Ibata, R. 2009, MNRAS, 396, 1231
Rey, M. P., & Starkenburg, T. K. 2022, MNRAS, 510, 4208
Rodriguez-Gomez, V., Pillepich, A., Sales, L. V., et al. 2016, MNRAS, 458, 2371
Roederer, I. U. 2009, AJ, 137, 272
Ruchti, G. R., Read, J. I., Feltzing, S., et al. 2015, MNRAS, 450, 2874
Sandin, C. 2014, A&A, 567, A97
Searle, L., & Zinn, R. 1978, ApJ, 225, 357
Sesar, B., Jurić, M., & Ivezić, Ž. 2011, ApJ, 731, 4
Shen, J., Rich, R. M., Kormendy, J., et al. 2010, ApJL, 720, L72
Seth, A., de Jong, R., Dalcanton, J. & GHOSTS Team 2007, IAUS, 241, 523
Shi, R., Wang, W., Li, Z., et al. 2022, MNRAS, 515, 3938
Sick, J., Courteau, S., Cuillandre, J.-C., et al. 2015, IAUS, 311, 82
Smercina, A., Bell, E. F., Samuel, J., & D'Souza, R. 2022, ApJ, 930, 69
Smercina, A., Bell, E. F., Price, P. A., et al. 2020, ApJ, 905, 60
Smercina, A., Bell, E. F., Price, P. A., et al. 2023, ApJL, 949, L37
Sotillo-Ramos, D., Pillepich, A., Donnari, M., et al. 2022, MNRAS, 516, 5404
Szomoru, D., Franx, M., & van Dokkum, P. G. 2012, ApJ, 749, 121
Szomoru, D., Franx, M., van Dokkum, P. G., et al. 2010, ApJL, 714, L244
Tal, T., & van Dokkum, P. G. 2011, ApJ, 731, 89
Tanaka, M., Chiba, M., Komiyama, Y., Guhathakurta, P., & Kalirai, J. S. 2011, ApJ, 738, 150
Tikhonov, N. A., & Galazutdinova, O. A. 2005, Ap, 48, 221
Trujillo, I., & Fliri, J. 2016, ApJ, 823, 123
Trujillo, I., D'Onofrio, M., Zaritsky, D., et al. 2021, A&A, 654, A40
van Dokkum, P. G., Abraham, R., & Merritt, A. 2014, ApJL, 782, L24
Viswanathan, A., Byström, A., Starkenburg, E., et al. 2026, A&A, 706, A195
Wang, J., Navarro, J. F., Frenk, C. S., et al. 2011, MNRAS, 413, 1373
Wang, W., Han, J., Sonnenfeld, A., et al. 2019, MNRAS, 487, 1580
Wang, W., Li, X., Shi, J., et al. 2021a, ApJ, 919, 25
Wang, W., Takada, M., Li, X., et al. 2021b, MNRAS, 500, 3776
Watkins, L. L., Evans, N. W., Belokurov, V., et al. 2009, MNRAS, 398, 1757
Wetterer, C. J., & McGraw, J. T. 1996, AJ, 112, 1046
White, S. D. M., & Rees, M. J. 1978, MNRAS, 183, 341
Williams, B. F., Dalcanton, J. J., Bell, E. F., et al. 2015, ApJ, 802, 49
Williams, D. J., Damjanov, I., Sawicki, M., et al. 2025, ApJ, 989, 107
Woltjer, L. 1975, A&A, 42, 109
Xiang, M., & Rix, H.-W. 2022, Natur, 603, 599
Xu, Y., Liu, C., Xue, X.-X., et al. 2018, MNRAS, 473, 1244
Xue, X.-X., Rix, H.-W., Ma, Z., et al. 2015, ApJ, 809, 144
Yang, C., Zhu, L., Tahmasebzadeh, B., Xue, X.-X., & Liu, C. 2022, AJ, 164, 241
Yanny, B., Newberg, H. J., Grebel, E. K., et al. 2003, ApJ, 588, 824
Youakim, K., Starkenburg, E., Martin, N. F., et al. 2020, MNRAS, 492, 4986
Zaritsky, D., Golini, G., Donnerstein, R., et al. 2024, AJ, 168, 69
Zhang, H.-X., Puzia, T. H., & Weisz, D. R. 2017, ApJS, 233, 13
Zibetti, S., White, S. D. M., & Brinkmann, J. 2004, MNRAS, 347, 556